

# Imaging Polarimetry of Human Eye

Masahiro Miura

(Doctoral Program in *Applied Physics*)

Submitted to the Graduate School of

Pure and Applied Sciences

in Partial Fulfillment of the Requirements

for the Degree of Doctor of Philosophy in

*Engineering*

at the

University of Tsukuba



*To my beloved family:  
Tensho, Hikari,  
and my dear wife Kiwa*



# Acknowledgments

I would like to thank my supervisor, Prof. Masahide Itoh. Without his support and guidance, this work would not have been possible. I deeply appreciate Prof. Ann E. Elsner, a preceptor for the postdoctoral fellowship at the Schepens Eye Research Institute, who introduced me to the fascinating world of applied optics. She is now in Indiana University, and I truly feel fortunate to continue my fruitful collaboration with her group. I am grateful to have made my acquaintance with the Computational Optics Group at the University of Tsukuba. Dr. Yoshiaki Yasuno, Dr. Shuichi Makita, and Dr. Masahiro Yamanari introduced me to the wonderful world of optical coherence tomography. The method of OCT, which I learned under the guidance of Dr. Yasuno has captivated me. Dr. Makita taught me how to solve complicated riddles in the field of applied optics. Without Dr. Yamanari's PS-OCT method, I could not have finished this work. I truly appreciate Prof. Masahiko Usui, Prof. Hiroshi Goto, and Prof. Takuya Iwasaki from Tokyo Medical University for encouraging me to continue with this study. Finally, I want to dedicate this study to my family and parents for their selfless support.

*Masahiro Miura*



# Table of Contents

<b>Abstract of dissertation</b>	<i>Page 9</i>
<b>Chapter 1.</b>	
<b>Introduction</b>	<i>Page 11</i>
<b>Chapter 2.</b>	
<b>Polarization measurement of the anterior segment of the human eye in vivo.</b>	
Abstract	<i>Page 13</i>
2-1. Introduction	<i>Page 14</i>
2-2. Samples	<i>Page 14</i>
2-3. Polarization-sensitive swept-source OCT	<i>Page 14</i>
2-4. Polarization measurement	<i>Page 16</i>
2-5. Discussion and Conclusion	<i>Page 17</i>
<b>Chapter 3.</b>	
<b>Polarization measurement of the posterior segment of the human eye in vivo with polarization-sensitive scanning laser ophthalmoscope</b>	
Abstract	<i>Page 23</i>
3-1. Introduction	<i>Page 24</i>
3-2 Polarization-sensitive scanning laser ophthalmoscope	<i>Page 25</i>
3-3. Polarimetry images	<i>Page 26</i>
3-4. Polarimetry images of normal eye	<i>Page 27</i>
3-5. Imaging polarimetry in central serous chorioretinopathy	
3-5-1. Introduction	<i>Page 30</i>
3-5-2. Samples	<i>Page 30</i>
3-5-3. Results	<i>Page 31</i>
3-5-4. Discussion and Conclusion	<i>Page 32</i>
3-5-5. Summary	<i>Page 33</i>
3-6. Imaging polarimetry and retinal blood vessel quantification at the epiretinal membrane	
3-6-1. Introduction	<i>Page 36</i>
3-6-2. Samples	<i>Page 37</i>
3-6-3. Analysis of vessel quantification	<i>Page 38</i>

3-6-4. Results	<i>Page 39</i>
3-6-5. Discussion and Conclusion	<i>Page 40</i>
3-6-6. Summary	<i>Page 41</i>
<b>Chapter 4.</b>	
<b>Combination of PS-SLO and PS-OCT for the posterior segment of the human eye in vivo</b>	
Abstract	<i>Page 49</i>
4-1. Introduction	<i>Page 50</i>
4-2. Polarization-sensitive spectral-domain optical coherence tomography	<i>Page 51</i>
4-3. Samples	<i>Page 52</i>
4-4. Normal eyes	<i>Page 53</i>
4-5. Eyes with macular disease	<i>Page 57</i>
4-6. Discussion and Conclusion	<i>Page 59</i>
4-7. Summary	<i>Page 61</i>
<b>Chapter 5.</b>	
<b>Conclusion</b>	<i>Page 69</i>
<b>References</b>	<i>Page 71</i>



# Abstract of the dissertation

Optical imaging is an important technique for evaluating the human eye. Polarization analysis has long been used for evaluating human tissues. The polarization properties of the retinal nerve fiber layers have been well studied; however, little is known about the polarization properties of other ocular tissues. The optical performance of the entire eye depends to some extent on the polarization properties of individual elements, and the polarization properties of abnormal tissues should be different from those of normal ocular tissues. We studied the polarization properties of various ocular tissues and investigated various possibilities for the application of optical imaging.

Polarization-sensitive swept-source optical coherence tomography (PS-SS-OCT) at 1.3  $\mu\text{m}$  was used to measure the polarization properties of the anterior segment of the human eye. With PS-SS-OCT, the boundary of the sclera could be easily distinguished, and the thickness of the sclera could be accurately measured. In the eye with necrotizing scleritis, birefringence at the sclera was low in diffuse areas; this implied that diffuse destruction of the collagen fibers had occurred in the sclera. PS-SS-OCT is an effective tool for understanding the polarization properties of the anterior eye segment and is useful in evaluating anterior eye segment disorders.

Polarization-sensitive scanning laser ophthalmoscope (PS-SLO) at 780 nm was used to measure the polarization properties of the human retina. We computed the following 4 polarimetric images: the average reflectance image, the parallel polarized light image, the phase-retardation map, and the depolarized light image. First, PS-SLO was used to evaluate the multiple-scattering light from the deep retinal lesions in central serous chorioretinopathy. In the depolarized light image, the leakage areas presented as high-intensity areas, indicating a high degree of multiple scattering of the returning light at those locations, which in turn suggested a disorder of the local tissues. Depolarized light images are useful for the noninvasive assessment of retinal disorders. Next, PS-SLO was used to examine retinal blood vessels in a retinal area containing epiretinal membrane. In the presence of membrane formation on the retinal surface, interference was observed in the polarization-insensitive images of the retinal vasculature; however, the depolarized light images clearly depicted the retinal vasculature. This result suggests that the polarimetric method is an effective tool for visualizing retinal vessels in eyes with retinal disease.

A combination of PS-SLO and PS- OCT offers a variety of possibilities for diagnosis. PS-SLO is useful for selectively studying the different layers of the retina.

PS-OCT allows collection of three-dimensional information on the polarization properties of the retina. We compared PS-SLO and polarization-sensitive spectral domain OCT (PS-SD-OCT) at 840 nm to evaluate the polarization properties of the human retina. The PS-SLO is an effective system for easily obtaining the polarization state at the region of interest, and provides information on multiple-scattered light as well as birefringence. With PS-SD-OCT, the origin of the polarization change could be easily detected, and more information on the polarization properties of the diseased retina could be obtained. A combination of PS-SLO and PS-SD-OCT is an effective tool for understanding the polarization properties of the retina.

# Chapter 1

## Introduction

The human eye is a unique organ for study in the field of applied optics. The layers of tissues present in the optical pathway to the photosensors, the so-called photoreceptors, are transparent so that they facilitate the passage of visible light. The presence of these clear tissues makes the human eye an optimal organ for assessment with an optical instrument, and optical imaging is an important technique for evaluating the human eye. Various optical properties, such as the spectrum<sup>1,2</sup>, refraction<sup>1,3</sup>, and polarization<sup>4</sup>, have been used to evaluate the human eye. The polarization properties of the retinal nerve fiber layers<sup>5,6,7</sup> have been well studied; however, little is known about the other ocular tissues. The photoreceptors in the human eye were shown to be insensitive to polarization changes; therefore, polarization measurement has received little attention. The optical performance of the entire eye depends to some extent on the polarization properties of individual elements; moreover, the polarization properties of abnormal tissues should be different from those of normal ocular tissues. Polarization measurement is an important technique for evaluating the microstructures of biological elements<sup>4,8</sup>. We studied the polarization properties of various ocular tissues were studied and evaluated the possibilities for the application of optical imaging.

Chapter 2 describes the evaluation of the polarization properties of the anterior segment of the human eye. Polarization-sensitive swept-source optical coherence tomography (PS-SS-OCT) at 1.3  $\mu\text{m}$  was used for the polarization measurement. With PS-SS-OCT, the boundary of the sclera could be easily distinguished, and the thickness of the sclera could be accurately measured. In the eye with necrotizing scleritis, birefringence at the sclera was low in diffuse areas; this implied that diffuse destruction of the collagen fibers had occurred in the sclera. We showed that PS-SS-OCT is an effective tool for understanding the polarization properties of the anterior eye segment and that it is useful in evaluating anterior eye segment disorders.

Chapter 3 describes the evaluation of the polarization properties of the human retina with a polarization-sensitive scanning laser ophthalmoscope (PS-SLO) at 780 nm. We computed the following 4 polarimetric images: the average reflectance image, the parallel polarized light image, the phase-retardation map, and the depolarized light image. First, PS-SLO was used to evaluate the multiple-scattering light from the deep retinal lesions in central serous chorioretinopathy. In the depolarized light image, the leakage

areas presented as high-intensity areas, indicating a high degree of multiple scattering of the returning light at these locations, which in turn suggests the presence of a local tissue disorder. From these studies with PS-SLO, we showed that the detection of depolarization is useful as a noninvasive assessment of retinal disorders. Next, PS-SLO was used to examine the retinal blood vessels in a retinal area containing epiretinal membrane. In normal eyes, the degree of contrast between the retinal arteries and veins was higher in the 514-nm images. In the presence of membrane formation on the retinal surface, interference was observed on the 514-nm polarization-insensitive retinal vascular images; moreover, the depolarized light image clearly depicted the retinal vasculature. This result suggests that polarimetric methods are an effective tool for visualizing retinal vessels in eyes affected by retinal disease.

Chapter 4 describes the evaluation of the polarization properties of the human retina with a combination of PS-SLO and polarization-sensitive spectral-domain optical coherence tomography (PS-SD-OCT). The combination of PS-SLO and PS-SD-OCT offers a variety of possibilities for diagnosis. PS-SLO is useful for selectively studying the different layers of the retina. PS-SD-OCT allows the collection of three-dimensional retinal information with regard to the polarization properties. The PS-SLO is an effective system for easily determining the polarization state at the region of interest, and provides information on multiple-scattered light as well as birefringence. With PS-SD-OCT, the origin of the polarization change could be easily detected, and more information on the polarization properties of diseased retina was obtained. We showed that a combination of PS-SLO and PS-SD-OCT is an effective tool for understanding the polarization properties of the retina.

## Chapter 2

# Polarization measurement of the anterior segment of the human eye in vivo.

### Abstract

We developed a polarization-sensitive swept-source optical coherence tomography (PS-SS-OCT) system (central wavelength, 1310 nm; A-line rate, 20 kHz) and evaluated the three-dimensional structure of the anterior eye segment with the phase retardation associated with the anterior segment birefringence of the eyes. We evaluated normal eyes and an eye with necrotizing scleritis. In the sclera of the normal eyes, a striking polarization change was observed in the cumulative phase-retardation images, and the boundary of the sclera could be easily distinguished. In the eye with necrotizing scleritis, phase retardation in the sclera was low in an extensive area; this implied that diffuse destruction of the collagen tissue in the sclera had occurred. Polarization-sensitive OCT is useful as a contrast engine for the anterior eye segment and for the evaluation of pathological changes in the sclera.

## **2-1. Introduction**

The anterior segment of the human eye is an essential structure in the human optic organ (Fig 2-1). Cornea and lens are convex lenses to focus the light toward the center of the retina. Sclera covers the fragile internal tissues, and protects from the external pressures. Iris and ciliary processes are important structure to maintain the inner condition of eyeball. These structures are expected to have unique polarization properties. Cornea, sclera, and lens consist of microtubules, and might be birefringent. Pigment epithelial layers in iris and ciliary process contain melanin pigment, and might induce the multiply scattering light and the polarization scramble (depolarization). In this section, we evaluated the polarization properties of the human anterior segment.

The human sclera is an essential structure with important functions for the visual integrity of the eye<sup>9</sup>. Two-dimensional images of the anterior eye segment are readily obtained using ultrasound biomicroscopy<sup>10</sup> and time-domain optical coherence tomography (OCT)<sup>11</sup>. However, clinical application of these images for scleral disorders are restricted. Sclera is a comparatively uniform tissue, and an assessment of the microstructure of sclera was limited in these images. Sclera is a collagen rich tissue and induces birefringence<sup>12</sup>. The polarimetry technique might have some potential in evaluating the microstructure of the scleral disorders. In this study, we evaluated the microstructure of the sclera using a polarization-sensitive swept-source OCT (PS-SS-OCT).

## **2-2. Samples**

We compared an eye with necrotizing scleritis with 2 normal eyes of 2 healthy Japanese volunteers (2 males, age: 30 and 47 years). In case of necrotizing scleritis, we evaluated the right eye of a 60-year-old Japanese man with a history of rheumatoid arthritis. On ophthalmologic examination, irregularly shaped dark areas were observed on the anterior sclera.

## **2-3. Polarization-sensitive swept-source OCT**

The 1.3  $\mu\text{m}$  PS-SS-OCT system consists of the fiber-optic Mach-Zehnder interferometer as shown in Figure 2-2. The light source is a swept source (Santec

HSL-2000) sweeping at 20 kHz. A resonant electro-optic modulator (EOM) modulates the incident polarization sinusoidally with the frequency of 100/3 MHz with the amplitude of 2.405 radian. The Jones matrix of the EOM with the fast axis of  $\pi/4$  can be written as

$$\begin{pmatrix} \cos \varphi / 2 & i \sin \varphi / 2 \\ i \sin \varphi / 2 & \cos \varphi / 2 \end{pmatrix} \quad (1)$$

By applying Eq. (1) to the Jones vector of the vertically polarized light, the Jones vector of the light after at he modulation by the EOM is derived as

$$\begin{pmatrix} i \sin \varphi / 2 \\ \cos \varphi / 2 \end{pmatrix} \quad (2)$$

Since it is difficult to synchronize the resonant EOM and the swept source, they are driven asynchronously. The modulated beam is coupled to the single mode fiber. 10 % is directed to the reference arm and 90 % to the sample arm. In the reference arm, a linear polarizer (LP) and in-line polarization controllers (PC) have a role to obtain constant optical power and unchanged state of polarization independent to the incident polarization modulation by the EOM. For this purpose, a photodetector in the reference arm monitors the optical power. 99 % of the light to the sample arm illuminates the sample. 1 % of the light is directed to a mirror in order to calibrate the phase difference between the EOM and the data acquisition for each A-scan, because they are driven asynchronously. Back reflected light from the sample arm and the reference light are coupled to the polarization-maintaining fiber (PMF) and directed to the polarization-maintaining coupler (PMC). Fiber-optic polarizing beamsplitters (PBS) are attached in the two output ports of the PMC. Horizontally and vertically polarized signals are detected by the balanced photorecievers individually. A data acquisition board acquires the data at 100 M samples/s from each receiver. Similar to the method of time-domain PS-OCT with continuous polarization modulation, the detected signals have 0th and 1st order components due to the polarization modulation. The detected spectra are Fourier transformed and the 0th and 1st order components are windowed and extracted individually. The 1st order signal is shifted so that the 100/3 MHz matches the zero depth. The 0th order and the shifted 1st order signals are inverse Fourier transformed to the frequency domain. The spectra of the 0th and 1st order signals are rescaled in order to calibrate the nonlinearity of the frequency sweeping of the light source. The large difference of the refractive indices of the PMF causes the optical path length difference between the H and V channels. It is compensated numerically by introducing the 1st

order dispersion for the spectra of H and V channels individually. The mismatch of 2nd order dispersion between the reference arm and the sample arm is compensated numerically for all spectra. The compensated spectra are Fourier transformed again, and the depth-resolved signals are calculated. After simple calculation of the 0th and 1st order signals, all elements of the Jones matrices of the sample arm are calculated. Matrix diagonalization method is applied for the Jones matrices in order to compensate the birefringence of the fiber-optic components<sup>13</sup>. In this process, we calculate the phase retardation, diattenuation, and orientation of the sample.

The phase retardation was calculated by the Jones matrix based algorithm, and the phase retardation map of the eye was visualized as a depth-resolved image that was displayed on the scale of the conventional cross-sectional OCT intensity image. The transversal measurement area was 5.0 mm by 5.0 mm, and a raster scanning protocol from inferior to superior with 512 A-scans  $\times$  140 B-scans was used for all measurements of the polarization-sensitive swept-source OCT. The scanning rate was 20000 A scans/s and the acquisition time for the 3-dimensional image was 3.8 s. This system achieved 11.9  $\mu$ m axial image resolution in tissue. Cumulative phase retardation is displayed as grayscale, and grayscale 0-255 is equal to cumulative phase retardation 0-  $\pi$ . All investigations were performed using a protocol that adhered to the tenets of the Declaration of Helsinki and was approved by the Institutional Review Boards of the University of Tsukuba and Tokyo Medical University.

*(The portions of this chapter have been published in the following article:  
Yamanari M, Makita S, Yasuno Y. Polarization-sensitive swept-source optical coherence tomography with continuous source polarization modulation. Opt Express 2008;16:5892-5906.)*

## **2-4. Polarization measurement**

In the B-scan intensity images of both normal eyes and the eye with necrotizing scleritis, the boundaries between the scleras and conjunctivas were obscure (fig 2-3B, 2-4B). The scleras were observed as uniform highly reflective layers in both normal eyes and the eye with necrotizing scleritis, and information about the microstructures of the sclera could be hardly obtained. In the normal eyes, microstructures of ciliary processes were obscured by high scattering at the sclera (fig 2-3B). In the eyes with necrotizing scleritis, microstructures of ciliary processes could be clearly observed due to low scattering at the sclera (fig 1B). In the B-scan phase retardation images of the normal eyes, striking polarization changes were observed at these boundaries (fig 2-3C). Phase retardations were abruptly altered at the scleral boundary due to the presence of



birefringence at the sclera, and the boundaries between the sclera and conjunctiva could be easily detected. In the eye with necrotizing scleritis, phase retardation values at the sclera were low compared to normal eyes, and the polarization scramble at the pigment epithelium of the ciliary process could be detected (fig 2-4C). In some areas, birefringence at the sclera was observed, and the scleral boundary could be detected (fig 2-4C). We evaluated the *en face* cumulative phase retardation image at 0.3 mm beneath the scleral border. In the *en face* images of necrotizing scleritis, phase retardation was low in a wide area compared to normal eyes (fig 2-3D, 2-4D). Double-pass mean cumulative phase retardation values at these *en face* images were 224 and 236 deg for normal eyes, and 112 deg for the eye with necrotizing scleritis. The thickness of the sclera 2 mm posterior to the corneal limbus was 0.75 and 0.65 mm in case of the normal eyes, and 0.18 mm in case of the eye with necrotizing scleritis.

## **2-5. Discussion and Conclusion**

Two-dimensional images of the anterior eye segment are readily obtained using ultrasound biomicroscopy<sup>10</sup> and time-domain OCT<sup>11</sup>, however, three-dimensional information is limited due to the poor scanning speed of these systems. Recently, dramatic advances in OCT technology have enabled three-dimensional OCT imaging<sup>14</sup>. The 1310 nm wavelength swept-source OCT, which is a variation of the Fourier-domain OCT, allows three-dimensional imaging of the anterior segment<sup>15,16,17</sup>. In this study, we evaluated necrotizing scleritis using 1310 nm polarization-sensitive swept-source OCT, and analyzed the polarization properties by a non-invasive technique for the investigation of sclera. The B-scan OCT phase retardation image could provide information about the boundary and the internal microstructure of the anterior sclera, which could not be obtained by the conventional intensity-based OCT<sup>15,16,17</sup>. Detection of the boundary of the sclera is crucial for the interpretation of anterior segment images. Using polarization-sensitive swept-source OCT, the boundary of the sclera could be readily detected and an accurate measurement of the thickness of the sclera could be obtained. In the eye with necrotizing scleritis, birefringence at the sclera was low in diffuse areas; this implied that diffuse destruction of the collagen fibers had occurred in the sclera. Thickness of the sclera in the eye with necrotizing scleritis was markedly low compared to that of the sclera in the normal eyes. Detections of the destruction of collagen fibers and thinning of the sclera are important indicators of the severity of the scleritis, and polarization-sensitive swept-source OCT could be the ideal tool for the evaluation of the pathological change in the sclera. Polarization-sensitive swept-source OCT is an

effective tool to understand the polarization properties of the anterior eye segment and is useful in evaluating anterior eye segment disorders.

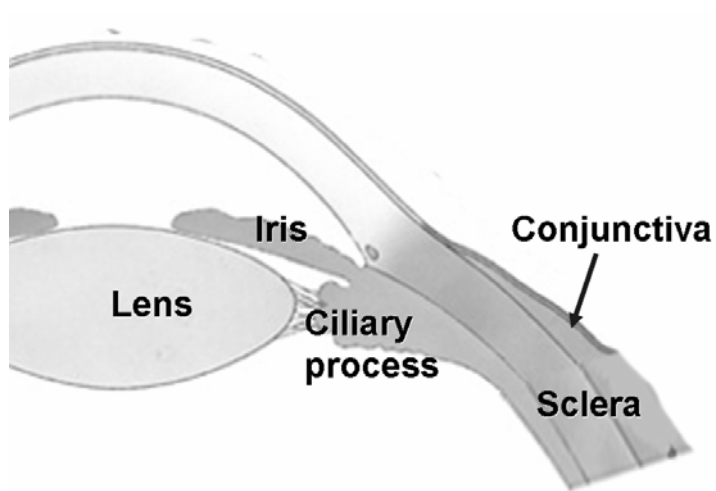


Figure 2-1  
 Schema of anterior segment of the human eye

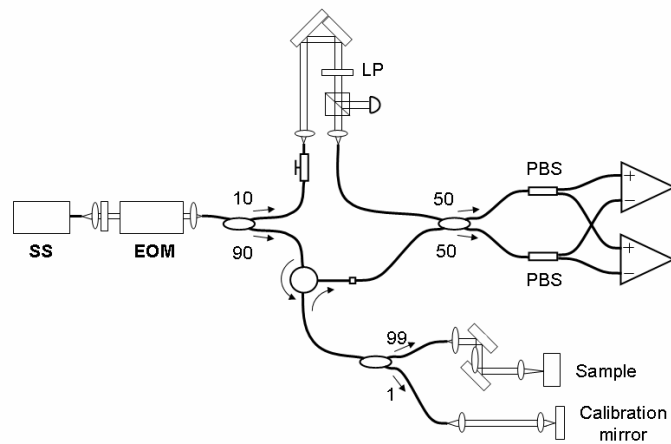


Figure 2-2  
 Schema of polarization-sensitive swept-source optical coherence tomography. SS: swept source, EOM; electro-optic modulator, LP: linear polarizer, PBS Fiber-optic polarizing beamsplitter

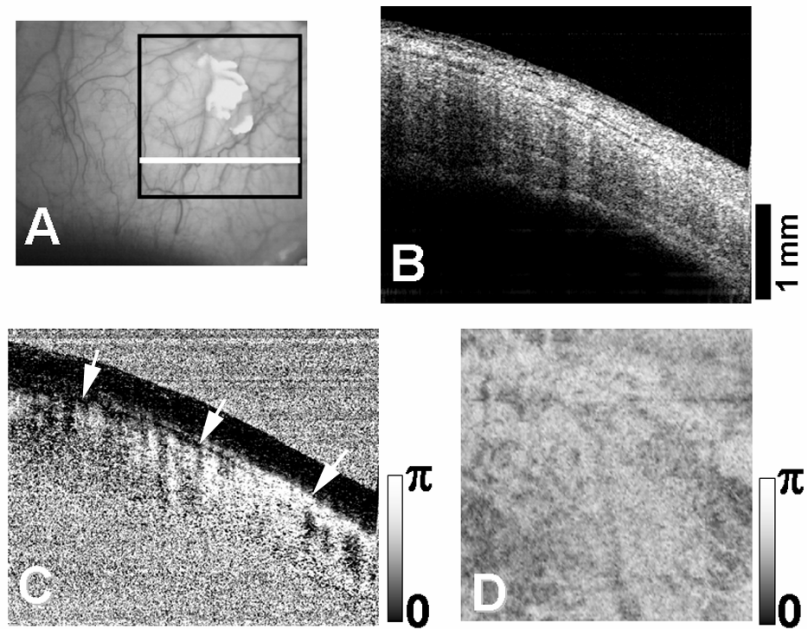


Figure 2-3

Healthy left eye of a 47-year-old male. A) The white line indicates the scanning line for the B-scan OCT images in Fig 2-3B and 2-3C. The black line indicates the area of the OCT imaging in Fig 2-3D. B) B-scan intensity image. C) B-scan cumulative phase retardation image. Striking polarization change was observed at the scleral border. (white arrows). D) *En face* cumulative phase retardation image at 0.3 mm beneath the scleral border.

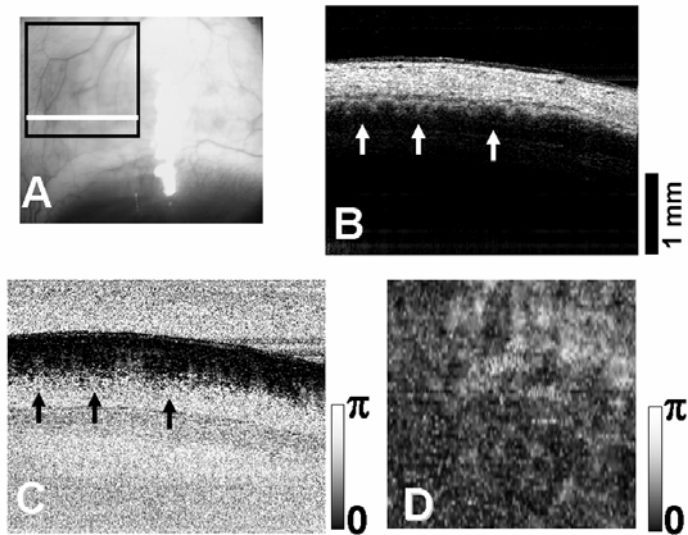


Figure 2-4.

Right eye of a 60-year-old male with necrotizing scleritis. A) The white line indicates the scanning line for the B-scan OCT images in Fig 2-4B and 2-4C. The black line indicates the area of the OCT imaging in Fig 2-4D. B) B-scan intensity image. White arrows indicate the ciliary process. C) B-scan cumulative phase retardation image. Polarization scramble at the pigment epithelium of the ciliary process could be detected (black arrows). D) *En face* cumulative phase retardation image at 0.3 mm beneath the scleral border (Fig 2-4D).



## Chapter 3

# Polarization measurement of the posterior segment of the human eye in vivo with polarization-sensitive scanning laser ophthalmoscope.

### Abstract

A polarization-sensitive scanning laser ophthalmoscope (PS-SLO) at 780 nm was used to measure the polarization properties of the human retina. We computed the following 4 polarimetric images: the average reflectance image, the parallel polarized light image, the phase-retardation map, and the depolarized light image. First, PS-SLO was used to detect the multiple-scattering light from the deep retinal lesions in central serous chorioretinopathy. In the depolarized light image, the leakage areas presented as high-intensity areas, indicating a high degree of multiple scattering of the returning light at those locations, which in turn suggests the presence of disorders a local tissue disorder. Depolarized light images are useful as a noninvasive assessment tool for retinal disorders. Next, PS-SLO was used to examine retinal blood vessels in a retinal area containing epiretinal membrane. In normal eyes, the contrast between the retinal arteries and veins was higher in the polarization-insensitive images obtained at 514 nm. In the presence of membrane formation on the retinal surface, interference was observed in the 514-nm polarization-insensitive retinal vascular images; however, depolarized light images clearly depicted the retinal vasculature. This result suggests that polarimetric methods are an effective tool for visualizing retinal vessels in eyes with retinal disease.

### **3-1. Introduction**

The retina is one of the most important tissues in the human optical system. The retina includes a layer of photoreceptors. A photoreceptor converts the energy of incident photons into electric signals that are transmitted to the visual center of the brain. Diseases affecting the retina are a severe threat to the human visual system. The development of retinal imaging is therefore an essential part of the history of ophthalmology.

In 1851, Helmholtz demonstrated the principle of the ophthalmoscope by means of a simple optical device. His ophthalmoscope consisted of a semitransparent mirror that functioned to direct light from an external source into the subject's eye. This conventional optical instrument allowed the observation of light reflected at the fundus. The development of this device was one of the major advancements in ophthalmology.

However, ophthalmoscopy allows only qualitative observation of the eye. The retina consists of semi-translucent multi-layered tissues, and each layer has individual optical properties. Several optical models were proposed for explaining the light-tissue interaction in the human retina. A simple model of the healthy human retina<sup>3,18</sup> consists of a stack of layers containing well-ordered and contiguous cells and their processes. Several optical techniques such as spectrometry<sup>19</sup>, reflectometry<sup>3</sup>, and polarimetry<sup>5,20</sup> have been used to evaluate the optical property of each layer in the retina. A spectrometer was used to measure the spectral and spatial distribution of reflectance at each retinal layer<sup>19</sup>. This led to the development of the optical model of the retina and allowed a quantitative assessment of numerous parameters related to absorption and reflection by structures in the human eye. However, the efficacy of this method for evaluating retinal conditions is limited.

Light-retina interaction at the molecular level could not be measured with the spectrometer and reflectometer. Each retinal layer has individual polarization properties, and polarization measurement is expected to overcome this limitation and facilitate the evaluation of tissue architecture at the molecular level. Microtubule formation by nerve fibers and collagen fibers induces phase retardation. The thickness of the retinal nerve fiber layer is estimated by using the birefringent component of light returning from the ocular fundus<sup>5</sup>, since the light from the superficial structures retains a high degree of polarization. On the basis of this concept, images of the superficial structures of the fundus can be enhanced by using polarization-preserving light. In contrast, images of deep retinal lesions can be obtained by using the depolarized light remaining after the removal of the polarization-preserving light. Polarization measurement has the potential to evaluate microstructures; however, the human eye is insensitive to polarization changes, and polarization measurement has received little attention. In this chapter, we measured the polarization properties of the human retina by using polarization-sensitive scanning laser



ophthalmoscopy (PS-SLO) and attempted to establish new retinal imaging techniques.

### **3-2 Polarization-sensitive scanning laser ophthalmoscope**

We used data from a commercially available ellipsometer, GDx, with a fixed corneal compensator (Laser Diagnostic Technologies, San Diego, USA), which is an incomplete polarimeter with a confocal aperture of approximately 30 microns (Fig. 3-1). This instrument is a scanning laser ophthalmoscope that was originally developed for measuring the thickness of nerve fiber layers. Laser scans of the retina were obtained at 780 nm in a raster pattern, at a  $15 \times 15$  deg visual angle. Incident laser is linearly polarized with a linear polarizer, and the angle of polarization is controlled with the rotating half-wave plate. To minimize unrelated corneal birefringence, the GDx uses a fixed compensator with a magnitude of 60 nm and a polarization axis of 15 deg nasally downward (single-pass retardance), which is uniform across the pupil plane. The returning light is separated into 2 beams by a rotating polarizing beam splitter: light with the same polarization as the illumination light, digitized at the parallel polarized detector, and light polarized at 90 deg to the illumination light, digitized at the crossed detector. We obtained 20 image pairs that varied systematically with regard to the illumination polarization angle, and each image in the series was saved at a resolution of  $256 \times 256$  pixels with 8 bits of grayscale. The acquisition time for an image series was 0.7 sec.

### **3-3. Polarimetric images**

We computed polarimetric images from the 20 image pairs obtained<sup>21 22 23</sup>. The grayscale value of each image in the image series was corrected by using the spatially resolved offset and gain calibrations provided with each instrument. Next, all the images were aligned to correct for eye movements. We then calculated the image types representing a particular aspect of the reflectance of the retina (Fig. 3-2).

First, the average reflectance image was computed as the grand mean of the light returning to both detectors for all input polarization states. In the average reflectance image, the light returns either to the crossed or uncrossed detector, with no light component systematically removed. The grand mean of the light returning to both detectors for all the input polarization states was calculated as follows.

$$I_{AR} = (\sum (PPD_i + DPD_i))/40 \quad (3)$$

where  $I_{AR}$  is the light intensity at each pixel averaged across images, PPD is the light intensity for the parallel polarized detector, and DPD is the intensity distribution for the perpendicularly polarized detector ( $i = 1, 20$ ). This value represents the average relative reflectance of the retina or, conversely, the relative reflectance that would be measured with a polarization-insensitive detection channel and a randomly polarized light source. This image represents the image obtained with a typical confocal scanning laser ophthalmoscope.

Second, the parallel polarized light image was computed. This value represents the average of amount of light, reaching the parallel detector that retains its original polarization, with the amplitude displayed in grayscale and independent of input polarization angle. The parallel polarized light image was calculated as the average intensity for the parallel polarized light minus the depolarized light contribution to each pixel.

$$I_{PP} = (\sum (PPD_i))/20 - \min[F(\alpha)] \quad (4)$$

where  $I_{PP}$  is the parallel polarized light intensity at that pixel, PPD ( $i = 1, 20$ ) is the total intensity for the parallel polarized detector.  $F$  is the intensity function of the crossed detector for all images in a set,  $\alpha$  is the angle of input polarization, and  $\min$  is the minimum of the function. This value represents the average amount of light that retains its original polarization, independent of the input polarization.

Third, the phase retardation map was computed from the modulation of the light returning to the crossed detector. We calculated the phase-retardation map, which represents input polarization-dependent change in intensity as

$$I_{PRM} = \max[F(\alpha)] - \min[F(\alpha)] \quad (5)$$

Max is the maximum of the function. In this image, regions of the retina where the polarization of the returning light is most dependent on the polarization of the illumination light are represented as high-intensity areas.

Finally, we computed the distribution of depolarized light (the depolarized light image), which is the minimum value of light detected for the crossed detector and all the input polarization angles, as follows.

$$I_{DP} = \min[F(\alpha)] \quad (6)$$

where  $I_{DP}$  is the depolarized light intensity at that pixel.

The intensities of the computed polarimetry images varied widely, and as expected, the depolarized light images and the phase-retardation map were too dark for subjective evaluation without further manipulation. For better visualization, the distribution of intensities in each image was adjusted as follows: minimum to maximum intensities in the images were converted to a grayscale range of 0–255 grayscale units.

### **3-4. Polarimetric images of the normal eye**

In the polarimetric images of the normal subjects, images differing in polarization content emphasized different aspects of the features of the eye (Fig. 3-3). The average reflectance images clearly showed high-degree reflections at the center of the major retinal vessels; this finding is typical of confocal images. Phase-retardation maps showed the expected macular bow-tie pattern attributable to the interaction of corneal and foveal birefringence, and a systematic radial change in birefringence. Superficial features, such as the reflection at the center of the retinal vessels, were significantly reduced in the depolarized light images.

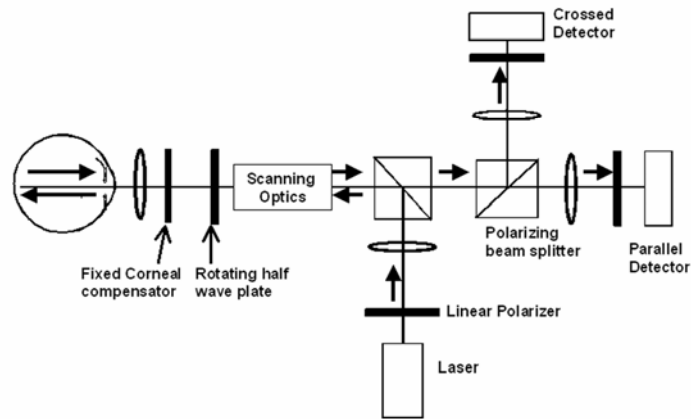


Figure 3-1:  
 Schema of polarization-sensitive scanning laser ophthalmoscope (GDx)

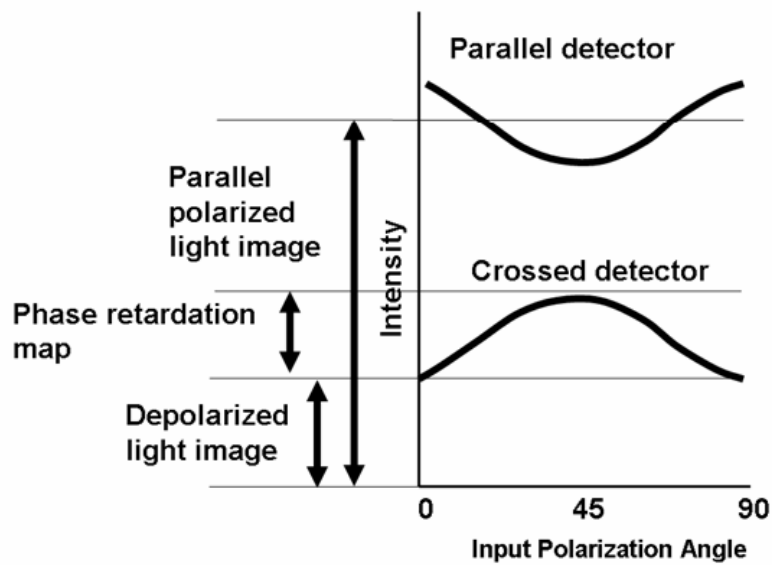


Figure 3-2:  
 Schematic diagram of the polarimetry algorithm that is used to compute different polarization content. The grayscale for one pixel is calculated of each 20 polarization angles.

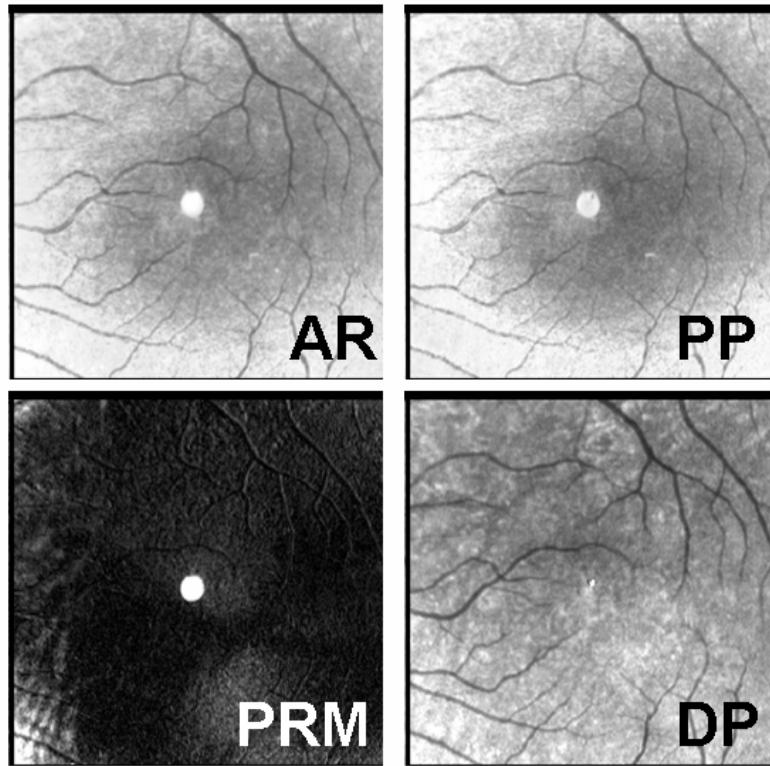


Figure 3-3

Computed polarimetry images of the normal eye. AR: average reflectance image, PP: parallel polarized light image, PRM: phase retardation map, DP: depolarized light image

## **3-5. Imaging polarimetry in central serous chorioretinopathy**

### **3-5-1. Introduction**

Central serous chorioretinopathy (CSR) is a common disorder that typically affects middle-aged adults, predominantly male, and is characterized by serous retinal detachment with leakage at the level of retinal pigment epithelium (RPE) <sup>24</sup>. The serous retinal detachment in CSR resolves spontaneously in most of the cases. In some cases, however, the resolution of the serous retinal detachments is delayed and patients may develop permanent visual loss <sup>24,25</sup>. For these cases, laser photocoagulation at the leakage point may be recommended, if the leakage points are located outside the fovea <sup>24</sup>. Localization of the leakage point is crucial for the treatment of CSR typically as ascertained in fluorescein angiography. Despite the widespread acceptance of fluorescein angiography, its application has been restricted due to the possibility of severe complication and the discomfort to patients <sup>26</sup>, as well as the time needed to perform the test. Thus, it is important to evaluate the potentiality of other techniques.

The morphological changes associated with CSR that occur at the leakage area in the deeper layers seen on histology, might induce the multiple scattering of the light, which would be detected in the depolarized light images. Further, the serous retinal detachment can be visualized on optical coherence tomography (OCT) <sup>27</sup>, and in some cases also the focal leakage area or changes to the retinal pigment epithelium, such as fibrinous exudates, are seen. We hypothesized that the polarimetry technique is useful to detect the leakage area in CSR without the injection of fluorescein dye. Further, the images may clearly denote the area of leakage and other features including fundus changes, occurring potentially in either acute or chronic CSR. In this study, we analyzed CSR with imaging polarimetry, which provides a method for the noninvasive assessment of CSR.

### **3-5-2. Samples**

We prospectively examined 30 eyes of 30 Japanese patients, 26 males and 4 females, 30 to 64 years (mean: 45.9 years), with CSR. Before testing, all patients received a detailed explanation of the study procedure and signed consent forms approved by the Institutional Review Board of Tokyo Medical University. The leakage area could be clearly localized in fluorescein angiography images in all eyes. The OCT images (Humphrey model 2000; Humphrey Instruments, San Leandro, USA) showed presence of serous retinal detachment in all eyes. In the OCT images, a small area of retinal pigment epithelial

detachment, corresponding to the area of dye leakage, was observed in 11 eyes, and a highly reflective lesion bridging the detached neurosensory retina and the retinal pigment epithelium was observed in one eye.

For the objective evaluation of the visibility of leakage area in polarimetry images, we calculated the contrast without any adjustment of intensities. We selected one leakage area from each eye. The average intensity of a  $4 \times 4$  pixels region of retina for the leakage area and the average intensity of the same size region adjacent to this area were both calculated. Michelson contrast was calculated for objective evaluation as follows:

$$\text{Michelson contrast} = (I_{\text{leakage}} - I_{\text{adjacent}}) / (I_{\text{leakage}} + I_{\text{adjacent}}) \quad (7)$$

where  $I_{\text{leakage}}$  was the average grayscale value on the leakage area and  $I_{\text{adjacent}}$  was the average grayscale value adjacent to the leakage area.

### **3-5-3. Results**

In the depolarized light images, the leakage areas could be clearly visualized as bright areas in all eyes (Figures 3-3). These bright areas were single bright dots in 3 eyes (Figures 3-3), and a single bright dot accompanied with multiple bright dots in 27 eyes (Figure 3,-4). However, in all eyes the leakage area could hardly be detected in the parallel polarized images, the average reflectance images, or the phase retardation map. The neurosensory retinal detachment was clearly localized as a large, dark area in the parallel polarized and average reflectance images, of similar or somewhat greater size compared with that seen in the depolarized light images, which emphasized the deeper layers. A bow-tie appearance in the phase retardation map was observed in 29 eyes (Figures 3-3), when present indicating the location of the fovea.

In 20 of the 30 eyes (67%), leakage areas were well defined in the depolarized light images (Fig. 3-3, 3-4), and showed sufficient quality for the guiding focal photocoagulation. In other 10 eyes (33%), leakage areas were surrounded by comparatively large bright spots, or relatively blurred. In these eyes, detection of the areas for focal photocoagulation was difficult in the depolarized light images.

For all cases, Michelson contrasts of the leakage area were  $0.58 \pm 0.28$  (depolarized light image),  $0.17 \pm 0.11$  (average reflectance image),  $0.09 \pm 0.09$  (parallel polarized light image), and  $0.11 \pm 0.21$  (phase retardation map). The Michelson contrasts for the depolarized light images were significantly higher than for the other three image types ( $P < .0001$ , for all tests, paired t-test).

### 3-5-4. Discussion and Conclusion

In the current study, we evaluated polarization analysis as a non-invasive technique for the evaluation of the extent of subretinal fluid and the localization of the pinpoint areas of light scattering in CSR. Polarization analysis could selectively emphasize the different features of the retina, visualizing more as opposed to less superficial layers depending upon polarization content. In the depolarized light image, the leakage areas presented as high intensity areas, indicating a high degree of multiple scattering of the returning light at those locations, in turn implying local tissue disorder. In recent OCT studies, various morphological changes at the leakage areas were reported, for example, pigment epithelial detachment<sup>27</sup>, a bridging lesion<sup>28</sup>, and bulges from RPE<sup>29</sup>. Our findings in the depolarized light image represent the morphological changes at the leakage areas, and agree with these OCT findings. In the chronic cases, CSR may be accompanied by RPE atrophy<sup>30</sup>, extensive pigmentary change<sup>30</sup>, or fibrinous exudates<sup>31</sup>. Multiple dots and high intensity area around the leakage area in the depolarized light images could provide important information about the RPE impairment around leakage areas.

The polarimetry technique has the advantage of being a non-invasive technique, which does not require pupil dilation, and provides *en face* results for a 15 deg region in one measurement. Testing time is short (0.7 s), and there is live viewing of the fundus during image acquisition to help ensure positive findings. The leakage point could readily be detected in the depolarized images without the need of repeated scans, so that existing treatment modalities could be applied with familiar landmarks. In some cases, the exact area for focal photocoagulation could not be determined, but an approximate area for photocoagulation might be obtained. Treatment outcomes based on the existing diagnostic and treatment modalities would then provide the necessary data as to the success of localization by polarimetry. Polarimetric analysis could also be useful tool as a preparatory test before fluorescein angiography.

The average reflectance and the parallel polarized images did not show the leakage areas as well as the depolarized light image, but did localize in high contrast the neurosensory retinal detachment. This was expected since the former two image types are generated by polarization preserving light, emphasizing more superficial structures. The average reflectance image is similar to an image of a confocal scanning laser ophthalmoscope, which has been shown to emphasize more superficial retinal structures. The contrast of the fluid surrounding the leakage areas in CSR is high in these image types because there is a reduction of transmission of light both into the and out of the fluid, accompanied by a loss of polarization of the light that does pass through. In addition, the average reflectance and parallel images have strong light return off the healthier regions of the retina, so that the resulting contrast with the darker region



of fluid is high.

The phase retardation map, which is generated from the modulation of the polarization preserving light, was not expected to enhance the visualization of key features of CSR. In 29 eyes of our case series, there was a macular bow-tie, which is due to the interaction of corneal and retinal birefringence<sup>32</sup>. The presence of a macular bow-tie implies incomplete correction for corneal birefringence by the fixed compensator, yet the presence of a macular bow-tie could help to localize the fovea. In CSR cases, the foveal reflex can be missing due to abnormal light-tissue interactions. Localization of the fovea can be useful when focal photocoagulation is being considered. Even in eyes with sufficient compensation for the corneal birefringence and absence of a macular bow-tie, this structure might easily be re-generated by tilting of the patient's head.

### **3-5-5. Summary**

In the current study, we evaluated polarization analysis as a non-invasive technique for the evaluation of the extent of subretinal fluid and the localization of the pinpoint areas of light scattering in CSR. Polarization analysis could selectively emphasize the different features of the retina, visualizing more as opposed to less superficial layers depending upon polarization content. In the depolarized light image, the leakage areas presented as high intensity areas, indicating a high degree of multiple scattering of the returning light at those locations, in turn implying local tissue disorder. Imaging polarimetry may assist with the rapid, noninvasive assessment of CSR.

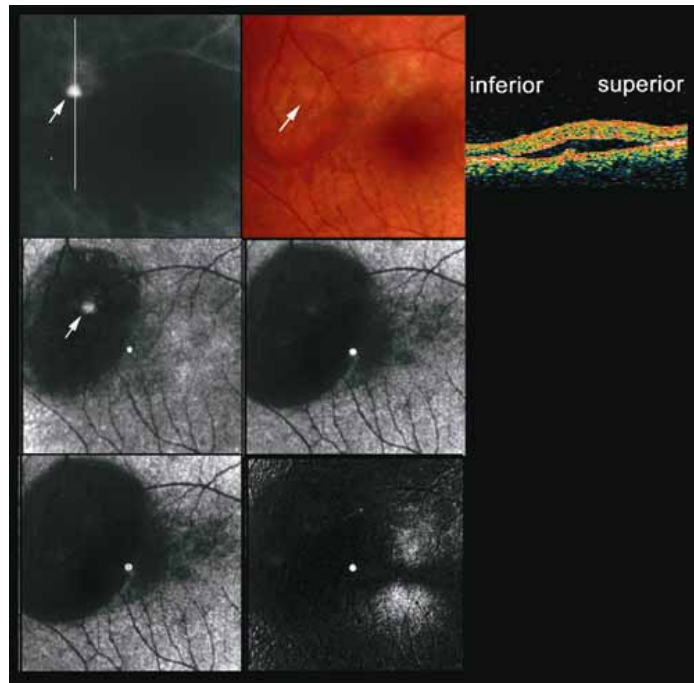


Figure 3-4:

Right eye of a 35-year-old man. Fluorescein angiogram (top left) demonstrating dye leakage temporal to the macula. The white line indicates the scanning line of the optical coherence tomography. Color fundus photograph (top center) showing a serous retinal detachment in the area temporal to the macula. Optical coherence tomography (top right), showing serous retinal detachment and a small retinal pigment epithelial detachment at the leakage area. A depolarized light image (middle left) clearly showing the leakage area as a bright dot (white arrow). A birefringence image (bottom right) showing the typical macular bow-tie. A parallel polarized light image (middle right) de-emphasizing the deeper features. An average reflectance image (bottom left) which shows the leakage area only faintly, but better shows the more superficial retinal features.

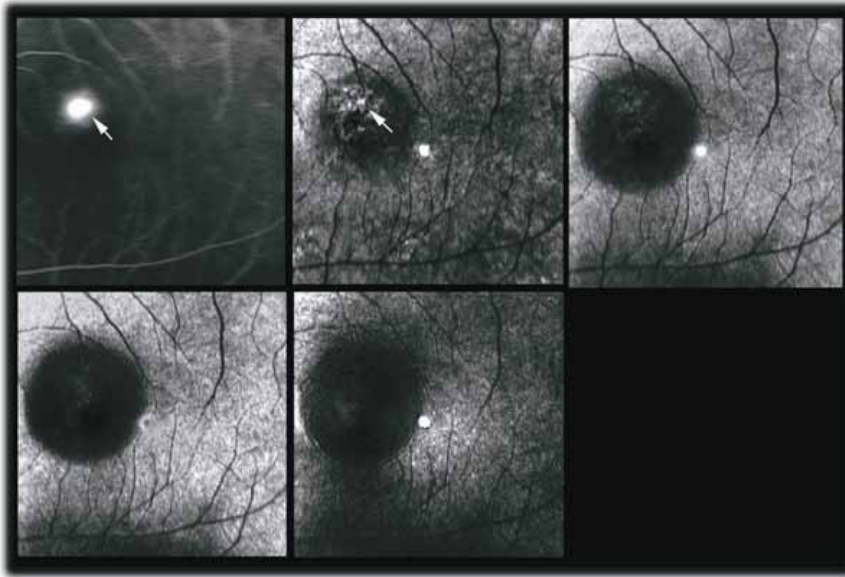


Figure 3-5:

Left eye of a 53 year-old-man. Fluorescein angiogram (top left) demonstrating dye leakage near the macula. A depolarized light image (top right) clearly showing the leakage point as a bright dot (white arrow) accompanied with multiple bright dots. In the birefringence image (bottom left), parallel polarized light image (bottom center), or average reflectance image (bottom right), the leakage area could be hardly detected.

## **3-6. Imaging polarimetry and retinal blood vessel quantification at the epiretinal membrane**

### **3-6-1. Introduction**

Epiretinal membranes (ERMs) are fibrocellular growths in the most superficial tissues of the retina<sup>33</sup>, commonly found in adults after the vitreous detaches from the retina. Contraction or shrinkage of ERMs causes varying degrees of visual disturbance, and the retinal vessels may be stretched or compressed along with the neural tissue. The presence of strong specular reflections from the gliotic tissue in an ERM leads to the retinal vasculature being obscured<sup>34</sup>. These and similar membranous formations are not uncommon findings in retinal disease, such as proliferative diabetic retinopathy, and interfere with the detection of retinal vascular pattern by the eye-care specialist or in automatic detection for screening. Even in the presence of poor image quality for the retinal vessels and lesion components, ERMs are routinely removed surgically by a variety of techniques<sup>35</sup>. With the retinal vascular pattern often poorly delineated, there is limited knowledge concerning potential ischemia or prospective estimation of improvement in vision. Both surgical success and subsequent visual improvement are variable, and improved diagnostic imaging may help overcome the reflection at ERMs and provide clear retinal vascular images.

In a variety of diseases with a retinal vascular component, accurate and reproducible detection of retinal blood vessels improves computer-based automatic detection of retinal disease, and biometrics for individual identification using retinal vascular pattern technology<sup>36</sup>. Optimal imaging and analysis techniques are required to obtain the clear images of the retinal blood vessels in the abnormal retina, since the complex light-tissue interactions are inherent in retinal vascular images<sup>37</sup>.

The wavelength of illuminating light in retinal images has been emphasized as a factor influencing the contrast of retinal vessels<sup>38 39</sup>. In a study using a monochromatic fundus camera, the small retinal blood vessels had good contrast at wavelengths between 510 nm and 570 nm<sup>39</sup>. Monochromatic images over a wide range of wavelengths, including the short wavelengths found in red-free photography, are readily obtained using SLO. Using an incident laser with a narrow spectral band in the short wavelength region, retinal vessels could be observed with high contrast. The illumination of only one point at a time prevents scattering over long distances from adjacent structures<sup>40</sup>. SLO images at short wavelengths can provide high contrast images of the retinal vessels<sup>41</sup>, but the contrast with near-infrared illumination approaches images with short wavelength illumination, and is far better than in flood illuminated fundus photography that lacks confocal apertures or adaptive optics. Short to medium wavelength illumination<sup>42</sup> that makes use of relatively high blood

absorption with respect to melanin absorption, rather than merely lights that appear blue, can produce excellent images in the presence of clear media, e.g. 514, 532, 543, or 595 nm<sup>40, 41</sup>

Another important factor is light-tissue interaction at the retinal blood vessel<sup>37, 43</sup>.  
44. Retinal vascular images are usually acquired using double-pass equipment. Returning light is a function of reflected, backscattered, and absorbed light from the fundus. Absorption by blood in a retinal vessel and backward multiple scattering from deeper layers are the main contributions to Beer's law, governing the potential contrast that can be obtained from retina vessels. The specular reflection at the retinal surface or retinal vessel wall can decrease the contrast of retinal vessels<sup>44</sup>. The most superficial layers of the retina and the vitreo-retinal interface provide a strong return of light relative to the deeper layers in a healthy eye, even with near infrared illumination<sup>45</sup>. With the presence of membranous formation at the retinal surface, the superficial layers of the retina become even stronger reflectors and obstruct retinal vascular images.

A polarimetry technique was developed to selectively emphasize the different components of light-tissue interactions at the retina, using an instrument that is highly confocal. Using an incomplete polarimeter, multiply scattered light returning from deeper layers could be emphasized by computationally removing the polarization preserving portion of the light returning from an image series that varies in input polarization. We assume that light that does not modulate with polarization angle has become randomly polarized due to multiple scattering. Using the depolarized light image, contrast of the retinal vessels is improved in two ways when compared with images in which the polarization content is not analyzed<sup>46 44</sup>. First, the unwanted specular reflex at the center of each vessel is eliminated, and higher contrast of the retinal vessels compared with the neighboring retina is obtained because there is no bright stripe that can merge into the edge of the retinal vessel, particularly with small to medium vessels. Second, the bright reflection from the vitreo-retinal interface and nerve fiber layer is also removed, which otherwise adds a globally bright signal across the retina, including over the blood vessels. In this study, we compared the effectiveness of visualizing the retinal vessels at ERMs with polarimetry images, as compared with SLO images at 514 nm. We hypothesize that 514 nm light images will provide high contrast images in the presence of clear media for normal subjects, and that the depolarized light images will have similar or only slightly worse contrast. However, in the presence of ERM, we hypothesize that the 514 nm images will no longer have the best contrast, and that the depolarized light images will provide better contrast.

### **3-6-2. Samples**

We prospectively examined 24 eyes of 24 Japanese patients, 8 males and 16 females, 51 to 79 years (mean: age 65.0 years), with ERMs. A group of age-matched normal subjects: 24 eyes of 24 Japanese subjects, age 49 to 80 years (mean: age 65.1 years) were also examined. There was no significance difference in age between ERM patients and normal subjects ( $P = 0.96$ , t-test). Eyes with any prior intraocular surgery were excluded from the study. All eyes had sufficiently clear media for obtaining good quality polarimetry images and SLO images at 514 nm. Before testing, all subjects received a detailed explanation of the study procedure and signed consent forms approved by the Institutional Review Board of Tokyo Medical University.

### **3-6-3. Analysis of vessel quantification**

For vessel quantification, we compared the average reflectance image, the parallel polarized light image, the depolarized light image, and the polarization insensitive image at 514 nm. For the polarization insensitive images, SLO images at 514 nm of 40 by 25 deg were digitized using the Rodenstock SLO (Rodenstock, Inc., München, Germany) with a confocal aperture of 800 microns with respect to the retina. Each image was manually aligned to the computed polarimetry images to have the same magnification as  $256 \times 256$  pixels with 8 bits of grayscale.

To calculate the contrasts of the retinal blood vessels, one retinal arteriole and one retinal venule were selected at 5 deg from the fovea of each eye. We selected those retinal vessel pairs large enough to provide sufficient samples for quantitative comparisons that could reach statistical significance. We used semi-automatic measurements of blood vessel intensity distribution (Fig. 3-6), but for this study modified the algorithm to allow analysis of images with a broader variety of file formats. This algorithm is based on the idea that blood vessels tend to have features that are longitudinally homogenous. An operator selected two points as the starting points, one on each side of a retinal vessel. The algorithm created 11 parallel lines along the line formed by the original two points, roughly perpendicular to the retinal vessel. Then the set of lines is rotated by  $\pm 20$  deg in 2 deg increments to optimize the vessel intersection angles. The Matlab algorithm did not resample the image during rotation, but rather placed each point in the sample for each of the 11 lines on the nearest pixel. For each of 11 parallel disector lines at given rotation angles, the minimum image intensity value is found, and its location over 11 bisector line is recorded. The algorithm then calculated the standard deviation of this location over the 11 lines. The perpendicular bisector line was defined as the angle that minimizes the standard deviation of the locations of the minimum values in bisector lines. Then the average blood vessel

profile was calculated (Fig. 3-6). The 11 bisector lines were averaged to reduce noise. Resampling of images occurred when figures were output for publication, which did not affect the computations.

To compare the retinal vessel profiles, we computed Michelson contrast of retinal vessels.

$$C = (L_{\max} - L_{\min}) / (L_{\max} + L_{\min}) \quad (8)$$

where C is the Michelson contrast of retinal vessel.  $L_{\max}$  is the average grayscale from the two most peripheral points on either side of the vessel profile, and  $L_{\min}$  is the average grayscale at the darkest point. Michelson contrasts were compared for each polarimetry image and SLO image at 514 nm, for normal subjects and patients, and for arteries and veins, with ANOVA and paired t-test.

### **3-6-4. Results**

In the normal retinas, clear retinal vascular images were obtained for each polarimetry image and SLO image at 514 nm (Fig. 3-7, 3-8). The reflections at the center of the retinal vessels were significantly reduced in the depolarized light images. In other images, the reflections at the center of the vessels were clearly observed at the major retinal arteries. In all eyes with ERMs, retinal vessels were clearly visible in the depolarized light images (Figs. 3-9, 3-10). More vessels were detectable, and these were uniformly dark in appearance. However, the retinal vessels had abnormal configurations, tortuous or stretched to the point of being straight. In other polarization image types shown, as well as the 514 nm images, the retinal vessels were considerably obscured by ERMs.

In normal eyes, the contrasts at retinal arteries and veins were significantly different according to image type (Fig. 3-11) ( $P < 0.0001$  for both arteries and veins, ANOVA). The order, from highest contrast to lowest was: 514 nm > depolarized > average > parallel. In ERM eyes, again the contrasts at retinal arteries and veins were significantly different according to image type (Fig. 3-12) ( $P < 0.0001$  for both arteries and veins, ANOVA). However, the order of contrasts at retinal arteries and retinal veins was different from that of normal subjects: depolarized > average > parallel > 514 nm. For normal subjects, the contrast in 514 nm images were significantly greater than in depolarized light images for retinal arteries and veins ( $P = 0.032, 0.001$ , respectively, paired t-test). For patients with ERM, the contrasts in depolarized light images were significantly greater than in the 514 nm light images for retinal arteries and veins ( $P < 0.001$  for arteries and veins, paired t-test).

### **3-6-5. Discussion and Conclusion**

In the current study, we evaluated polarization analysis as a non-invasive technique for the evaluation of retinal vascular changes visualized in image of ERMs. Polarization analysis can selectively emphasize different optical contributions from the retina. In the depolarized light images, the retinal vascular pattern in the presence of ERMs was readily visualized, indicating that detection of multiply scattered light is one way to improve retinal vascular imaging in the presence of ERMs.

The spectral properties of the illumination source have been discussed as important for retinal vascular images<sup>38,39</sup>. In the normal retina, retinal vessels were of high contrast with a SLO image with short wavelength illumination. With the presence of ERM, the same short wavelength yielded retinal vascular images with obstruction of the view of the vessels by membranous formation. This interference by membranous formation could be eliminated by using longer wavelength illumination, and contrast of retinal vessels could be improved. Among the images with near infrared illumination, the depolarized light image is better than average reflectance images and parallel polarized light images. The depolarized light image has a major contribution from multiply scattered light<sup>47,20</sup> from deep retinal layers, and the image of a dark retinal vessel on a lighter background depends upon on the Beer's law absorption of light that is passing through the blood as opposed to around the vessel. An ERM is a strong reflector, and the specular reflex at ERM forms an obstruction of clear retinal vascular images. The depolarized light image can eliminate the specular reflex at the retinal vessel, and also overcome the interference by ERM. Consequently, the depolarized light image at long wavelength illumination provides an improved imaging technique for visualizing retinal vessels in the same area as an ERM. Polarimetry images will allow more accurate measurement of absorption components of the light tissue interactions of the blood vessels at epiretinal membrane. This technique can help reduce the artifact or noise of the measurement of the optical properties at the retinal blood vessels, such as the reflection from the top of retinal vessels in oximetry<sup>37</sup>. Our method incorporates an incomplete polarimeter, which may not minimize the contribution of unwanted polarization-retaining light to the extent that full Mueller matrix polarimetry<sup>20</sup> could, has provided a related measurement of degree of polarization. Assuming that half the depolarized light reaches the crossed detector, and the other half reaches the parallel detector, then a pointwise estimate of ratio of depolarized light to the total is one image type of eighteen that we regularly compute. However, while subtracting from a unity image provides an image that is an estimate of degree of polarization, this type of computation confounds the two light components that we are trying to separate: 1) light retro-reflected



form deeper structures and passes through the blood vessels, and 2) light that returns mostly from more superficial structures. The GDx is a highly confocal instrument with a fixed corneal compensator<sup>48</sup>, which for a given image in the series provides nearly uniform polarization conditions to each point scanned on the retina. However, the GDx does not allow for variations of the confocal aperture size, which may be too small to optimize the contribution of scattered light in the depolarized light image<sup>49</sup>. Polarization methodologies that incorporate novel instrumentation or image analysis to emphasize specific data features or types of tissues, such as our method to enhance blood vessels by removing the unwanted specular reflections regardless of vessel orientation, polarization difference imaging, and new methods with principal components analysis.

### **3-6-6. Summary**

We studied a polarimetry method to examine retinal blood vessels in a retinal area containing epiretinal membrane. In normal eyes, contrasts of retinal arteries and veins were higher in 514 nm image. With a presence of membranous formation on the retinal surface, retinal vascular images were interfered in 514 nm images, and clear retinal vascular images were obtained with a depolarized light image. This result suggests, polarimetry methods are an effective tool for visualizing retinal vessels in eyes with retinal disease.

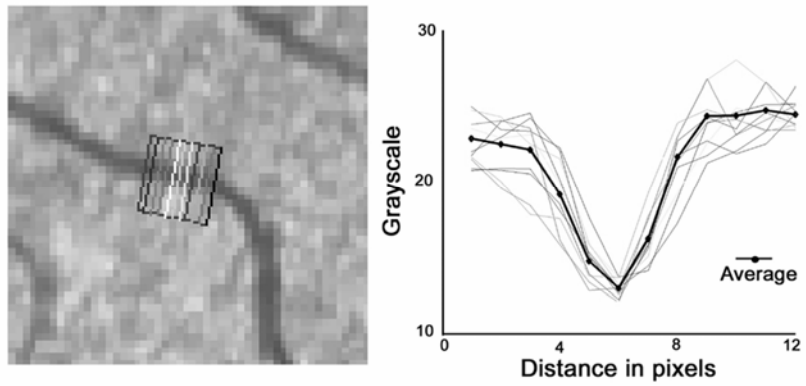


Figure 3-6

Vessel profiles across one artery in the depolarized light image of a normal subject. The 11 bisector lines were selected by a computer algorithm that finds adjacent parallel lines that are perpendicular to the vessel defined by selecting pixels on either side of the vessel (left). An average profile was calculated from the grayscale profile of 11 bisector lines (right).

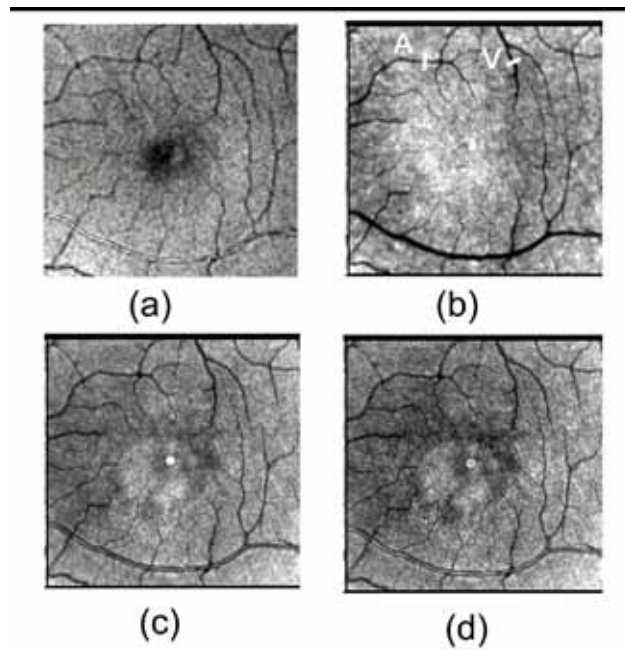


Figure 3-7

Retinal images of 66-year-old Japanese man with a normal retina. (a) 514 nm scanning laser ophthalmoscope image, (b) depolarized light images, (c) average reflectance image, (d) parallel polarized light image. A scanning laser ophthalmoscope image at 514 nm, average reflectance image, and average reflectance image demonstrating the reflection at the center of the major retinal artery. This reflection was significantly reduced in the depolarized light images. The bar indicates the sample region for vessel profiles of retinal artery (A) and retinal vein (V) in Figure 3-8. The bright spot in the center of each polarimetry image is an artifact due to internal reflections in the GDx.

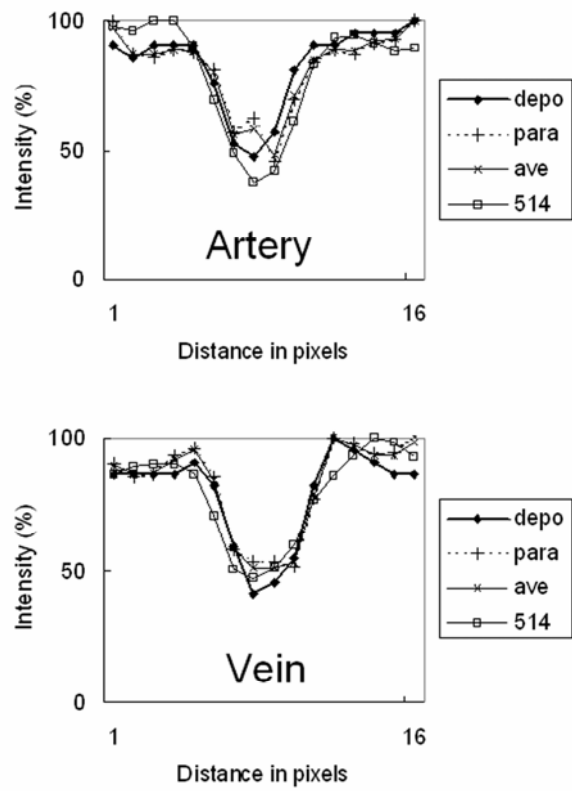


Figure 3-8

Computed data for blood vessel profiles of a retinal artery and a retinal vein, in the image of Figure 3-7. Each profile was plotted as % of maximum grayscale unit in each profile, as a function of location in profile.

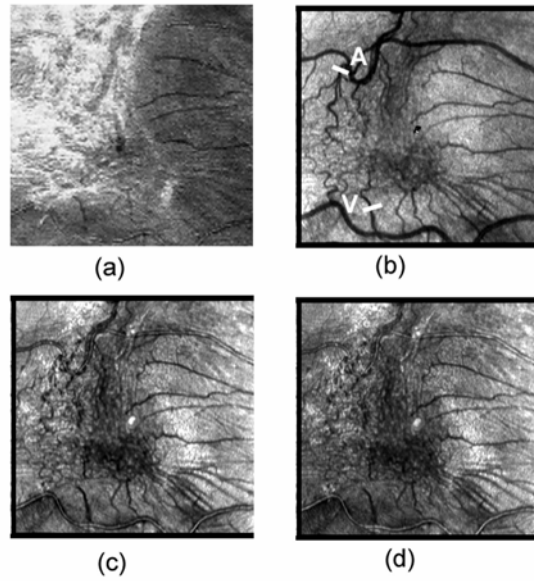


Figure 3-9

Retinal images of 70 year-old Japanese man with epiretinal membrane. (a) 514 nm scanning laser ophthalmoscope image, (b) depolarized light images, (c) average reflectance image, (d) parallel polarized light image. The epiretinal membrane could be clearly visualized as highly reflected area in the scanning laser ophthalmoscope image at 514 nm. In the depolarized light image, the retinal vessels could be clearly visualized in the area of epiretinal membrane. In the average reflectance image and parallel polarized light image, the retinal vessels were somewhat obscured by epiretinal membrane. The bar indicates the sample region for vessel profiles of retinal artery (A) and retinal vein (V) in Figure 3-10. The bright spot in the center of each polarimetry image is an artifact due to internal reflections in the GDx.

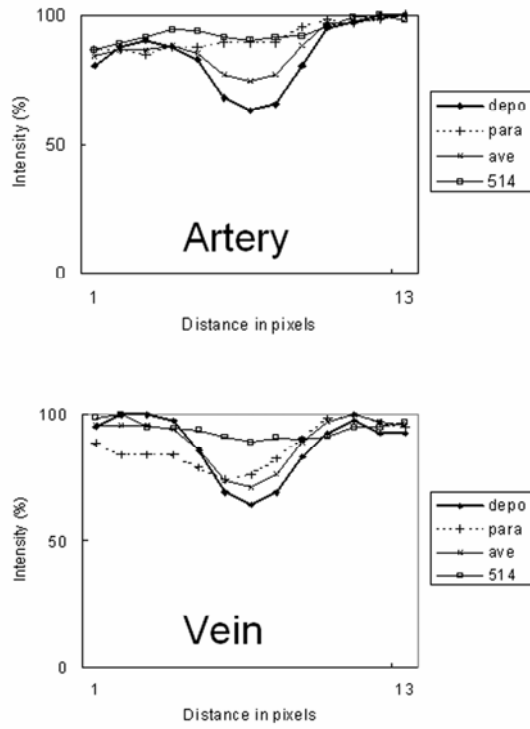


Figure 3-10

Computed data for blood vessel profiles of a retinal artery and a retinal vein, in the image of Figure 3-9. Each profile was plotted as % of maximum grayscale unit in each profile, as a function of location in profile.

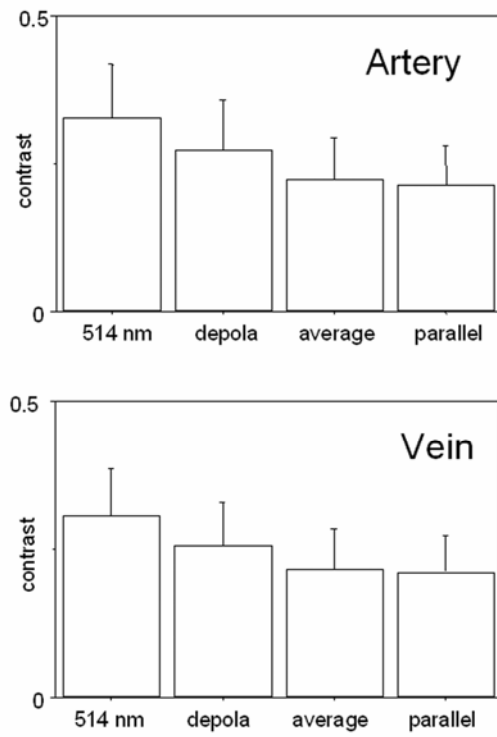


Figure 3-11

Michelson contrast of retinal arteries and veins in normal retinas. Contrast is greatest in SLO images at 514 nm. Error bars indicate standard deviation of Michelson contrast.

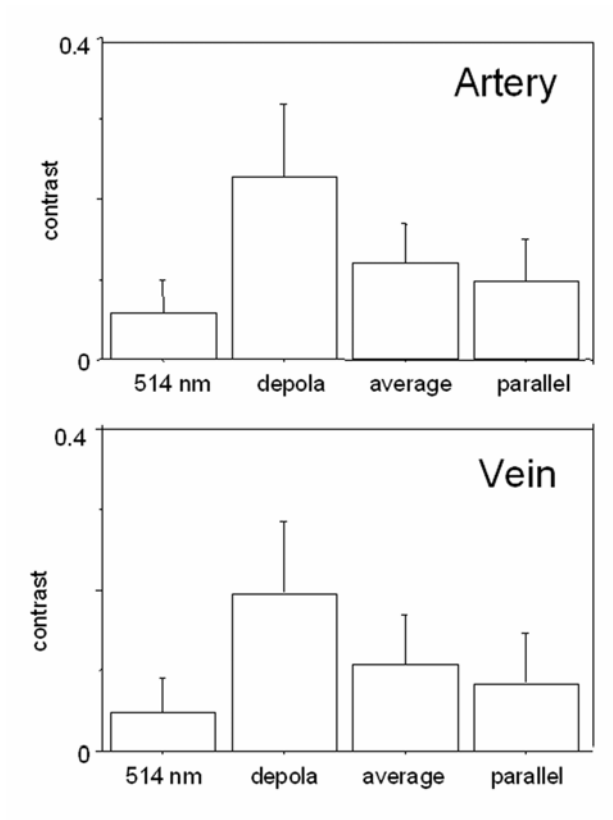


Figure 3-12  
 Michelson contrast of retinal arteries and veins in the eyes with epiretinal membranes. Contrast is greatest in the depolarized light image. Error bar indicate standard deviation of Michelson contrast.



## **Chapter 4**

# **Combination of PS-SLO and PS-OCT for the posterior segment of the human eye in vivo**

### **Abstract**

Combination of PS-SLO and PS- OCT offers a variety of possibilities for diagnosis. PS-SLO is useful to emphasize selectively the different layers of the retina. PS-OCT allows collection of three-dimensional retinal information about the polarization properties. We compared PS-SLO at 780 nm and polarization sensitive spectral domain OCT (PS- SD - OCT) at 840 nm to evaluate the polarization properties of the human retina. The PS-SLO is an effective system for easily obtaining the polarization state at the region of interest, and provides information concerning multiply scattered light as well as birefringence. With PS-SD-OCT, the origin of the polarization change could be readily detected, and could provide more information about polarization properties of retinal disease. A combination of PS-SLO and PS-SD-OCT is an effective tool to understand the polarization properties of the retina.

## 4-1. Introduction

Optical coherence tomography (OCT) is widely used imaging tool in ophthalmology<sup>50</sup>, especially for retinal disease accompanied by morphological changes, including AMD. Depth-resolved information about polarization has been obtained using polarization-sensitive OCT (PS-OCT)<sup>51, 8</sup>. Birefringence of the nerve fiber layer<sup>6</sup> and polarization scramble at the RPE<sup>52</sup> were measured with time-domain PS-OCT, but three-dimensional measurements were limited due to the scanning speeds of these systems. Recently, dramatic advances in OCT technology have facilitated improvements in three-dimensional PS-OCT measurements. Polarization-sensitive spectral-domain OCT (PS-SD-OCT)<sup>53, 54, 7</sup> allows three-dimensional retinal information about the polarization properties. Combination of scanning laser polarimetry and PS-SD-OCT offers a variety of possibilities for diagnosis. For instance, using the *en face* image of PS-SD-OCT, a direct comparison between scanning laser polarimetry and PS-SD-OCT is possible. Further, the origin of polarization changes in scanning laser polarimetry images can be detected and quantified with PS-SD-OCT. Structures seen in the scattered light images can be further probed in depth with PS-SD-OCT, to determine the spatial relation of highly reflective structures or increased birefringence seen in PS-SD-OCT to a focal increase in scattered light in scanning laser polarimetry.

Age-related macular degeneration (AMD) is a major cause of severe visual loss among older people in developed countries<sup>55</sup>. In AMD, the severe loss of central vision is often attributed to exudative lesions. Accurate investigation of exudative lesions is crucial for accurate evaluation and treatment of exudative AMD. Polarimetry techniques have been developed to emphasize selectively the different layers of the retina. PS-SLO has some potentiality to evaluate the macular disease. However, PS-SLO does not provide depth-resolved information about the polarization properties of the retina. Therefore, the depth of the origin of the polarization change has not yet been demonstrated. We compared PS-SLO images and PS-SD-OCT images of the same eyes to evaluate the birefringence properties of retinas with exudative AMD.

## 4-2. Polarization-sensitive spectral-domain optical coherence tomography

We used polarization-sensitive spectral-domain OCT (PS-SD-OCT) system. The light source is a superluminescent diode with a central wavelength of 840 nm, and bandwidth of 50 nm. The experimental axial resolution is 8.3  $\mu\text{m}$  in the air and 6.0  $\mu\text{m}$  in tissue. A polarization state of the probe beam is modulated by an EO modulator along B-scan. Two synchronized line-CCD cameras in a spectrometer allow high-speed measurement of horizontal and vertical polarization channels at line rate of 27.7 kHz. The sensitivity of the system is 101 dB. The power spectra detected by the two cameras are inverse Fourier transformed to obtain phase-resolved OCT signals for horizontally and vertically polarized components of the interfered light, respectively. The OCT signals are Fourier transformed along the lateral B-scan to extract the 0th and 1st order spatial frequency components, because each component is associated with different elements of the Jones matrix. These extracted spatial frequency components are individually inverse Fourier transformed. After calculation using these values, all the elements of the Jones matrix involving birefringence of the optical fiber, cornea, and retina are obtained. To compensate birefringence of the optical fiber and cornea, the Jones matrix is diagonalized using the signal at the retinal surface<sup>13</sup>. We assume the surface of the sample to be a mirror. Note that even if the surface tissue has birefringence, this algorithm is valid as long as the backscattering does not change the polarization. The Jones matrix at the surface of the sample can be expressed as

$$\mathbf{J}_{sur} = \mathbf{J}_{out} \mathbf{J}_{in} \quad (9)$$

where  $\mathbf{J}_{in}$  and  $\mathbf{J}_{out}$  are Jones matrices corresponding to the fiber components between the EO modulator and sample surface and that of the sample surface and polarizing beam splitter in the spectrometer, respectively.  $\mathbf{J}_{all}$  includes the round-trip Jones matrix of the sample  $\mathbf{J}_{sam}$ , i. e.,

$$\mathbf{J}_{all} = \mathbf{J}_{out} \mathbf{J}_{sam} \mathbf{J}_{in} \quad (10)$$

We can measure only  $\mathbf{J}_{offset} \mathbf{J}_{sur}$  and depth-resolved  $\mathbf{J}_{offset} \mathbf{J}_{all}$ . In order to obtain  $\mathbf{J}_{sam}$ ,  $\mathbf{J}_{in}$  is eliminated by multiplying  $\mathbf{J}_{offset} \mathbf{J}_{all}$  by  $(\mathbf{J}_{offset} \mathbf{J}_{sur} f)^{-1}$  and diagonalization is performed as

(11)

$$\begin{aligned}
\mathbf{J}_{all} \mathbf{J}_{surf}^{-1} &= \mathbf{J}_{offset} \mathbf{J}_{out} \mathbf{J}_{sam} \mathbf{J}_{in} (\mathbf{J}_{in}^{-1} \mathbf{J}_{out}^{-1} \mathbf{J}_{offset}^{-1}) \\
&= \mathbf{J}_{offset} \mathbf{J}_{out} \mathbf{J}_{sam} \mathbf{J}_{out}^{-1} \mathbf{J}_{offset}^{-1} \\
&= \mathbf{J}_U \begin{pmatrix} p_1 e^{i\delta/2} & 0 \\ 0 & p_2 e^{-i\delta/2} \end{pmatrix} \mathbf{J}_U^{-1}
\end{aligned}$$

where  $p_1$  and  $p_2$  are the attenuation coefficients of the sample;  $\eta$ , the retardation of the sample; and  $\mathbf{J}_U$ , an unitary matrix. We can calculate the relative optic axis, retardation, and diattenuation of the sample from this diagonalization. Retinal phase retardation is calculated from this Jones matrix based algorithm, and the phase retardation map of the eye is visualized as a depth-resolved image in addition to the conventional cross-sectional OCT intensity image.

The measurement area is 3.8 mm by 3.8 mm on retina, and a raster scanning protocol from inferior to superior with 1023 A-scans  $\times$  140 B-scans is used for all measurements of PS-SD-OCT. The experimental axial resolution is 8.3  $\mu\text{m}$  in the air and 6.0  $\mu\text{m}$  in tissue. The acquisition time for three-dimensional image was 5.5 sec. Data points corresponding to intensities below a criterion threshold are excluded in the phase retardation images. In the phase retardation images, the hue represents the phase retardation ranging from 0 deg to 180 deg, and the brightness represents the intensity of the OCT signals.

*(The portions of this chapter have been published in the following article: Yamanari M, Makita S, Madjarova VD, Yatagai T, Yasuno Y. Fiber-based polarization-sensitive Fourier domain optical coherence tomography using B-scan-oriented polarization modulation method. Opt Express 2006;14:6502-6515.)*

### 4-3. Samples

All investigations were performed using a protocol that adheres to the tenets of Declaration of Helsinki and was approved by the Institutional Review Boards of University of Tsukuba and Tokyo Medical University. For normal subjects, two healthy Japanese volunteers (2 males, age: 46 years and 26 years) without any detectable ocular disease were

selected. To evaluate exudative AMD, we prospectively examined 13 eyes of 13 Japanese patients, 10 males and 3 females, 51 to 82 years (mean: age 72.1 years) (Table 1). These cases include 5 cases of retinal pigment epithelial detachment, 3 cases of early stage of exudative AMD with predominantly classic choroidal neovascular membrane (CNV), one case of exudative AMD with retinal pigment epithelial tear, 3 cases of end stage of exudative AMD with disciform scar, and one case of recurrence of CNV after photodynamic therapy. All eyes had sufficiently clear media for obtaining good quality scanning laser polarimetry images and PS-SD-OCT images.

#### **4-4. Normal eyes**

The *en face* projection images generated from the three dimensional intensity OCT data showed a clear retinal vascular pattern (Fig. 4-2), and enables precise registration of PS-SD-OCT data with images from scanning laser polarimetry. In the intensity images of B-scan PS-SD-OCT, all retinal layers typical in high-resolution OCT could be observed (Fig. 4-3). In the cumulative phase retardation images of the B-scan PS-SD-OCT, hue and brightness show the phase retardation and intensity, respectively. In the normal retinas, the retardation image shows multiple layers of the brightness, which corresponds to the conventional OCT images of retina. However, hue of the retardation images in normal retina is constant throughout the retina except RPE layer, which means that the phase retardations were constant throughout these layers. Polarization scramble was observed at the RPE layer (Fig. 4-2F). The cumulative phase retardation values at intersection of inner and outer segments of photoreceptor in two normal subjects were 15 and 16 deg, respectively.

Table 1

Clinical characteristics in the patients with exudative AMD

Case	Age	Gender	Eye	Duration	VA	Exudative lesion	Figure
1	72 yr	F	R	1 wk	20/32	PED	Fig 4-3
2	51 yr	M	L	1 yr	20/100	PED	
3	81 yr	F	L	3 mo	20/32	PED	
4	82 yr	M	R	2 mo	20/50	PED	
5	81 yr	M	R	2 yr	20/400	PED	
6	75 yr	M	L	1 mo	20/40	early stage + predominantly classic CNV	Fig 4-4
7	71 yr	M	L	2 mo	20/40	early stage + predominantly classic CNV	
8	78 yr	M	R	1 mo	20/40	early stage + predominantly classic CNV	
9	57 yr	M	L	2 mo	20/25	CNV + RPE tear	Fig 4-5
10	75 yr	M	L	4 yr	20/200	disciform scar	Fig 4-6
11	74 yr	M	R	2 yr	20/200	disciform scar	
12	81 yr	F	R	5 yr	20/400	disciform scar	
13	66 yr	M	R	5 yr	20/200	disciform scar with new CNV	Fig 4-7

VA: best corrected visual acuity, PED: pigment epithelial detachment, CNV: choroidal neovascular membrane, RPE tear: retinal pigment epithelial tear

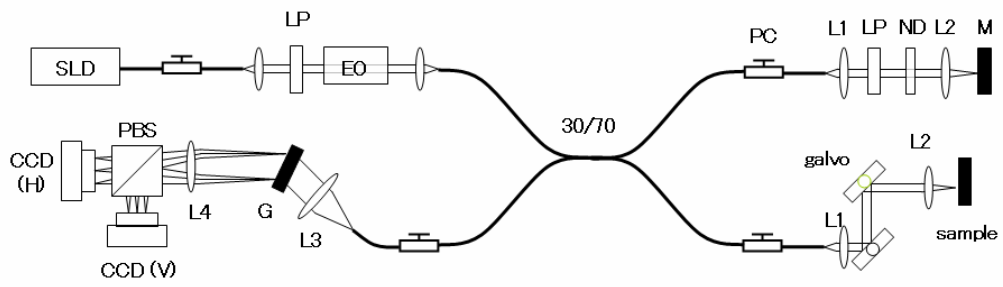


Figure 4-1.  
 Schema of polarization-sensitive spectral-domain optical coherence tomography.

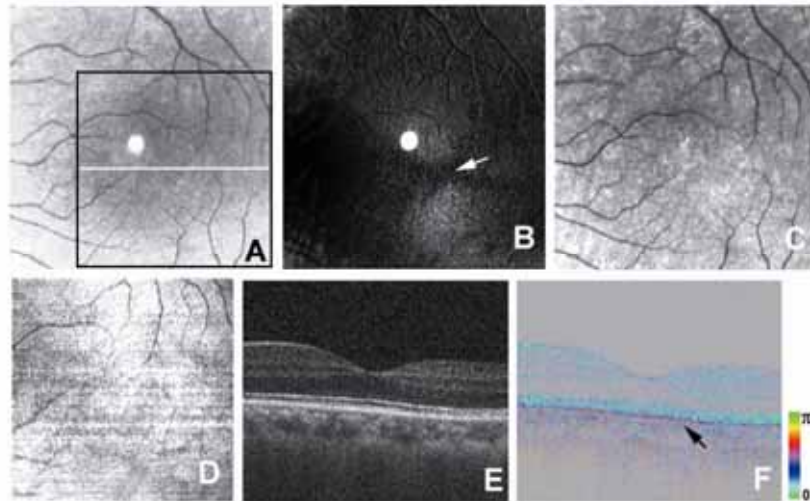


Figure 4-2

Left eye of a 46-year-old male with a healthy eye. (A) Average reflectance image of GDx. The black line indicates the area of PS-SD-OCT imaging in Fig. 4-2D. The white line indicates the scanning line for the B-scan PS-SD-OCT images in Figs. 4-2E and 4-2F. A bright spot on the center of the GDx image was an instrument artifact. (B) Phase retardation map of GDx. The white arrow indicates the center of macular bow-tie appearance. (C) Depolarized light image of GDx. (D) *En face* projection intensity image of PS-SD-OCT. (E) B-scan intensity image of PS-SD-OCT. (F) B-scan cumulative phase retardation image. The black arrow indicates the polarization scramble at the RPE layer.



## 4-5. Eyes with macular disease

For the exudative AMD, we evaluated a range of pathological changes, as described in the Methods section. In both PS-SLO and PS-SD-OCT, polarimetry findings in exudative AMD emphasized different aspects of features, and were related to the progression of the disease.

Five cases of retinal pigment epithelial detachments were evaluated for this study (Table 1, Figure 4-3). The color images showed retinal pigment epithelial detachments and surrounding exudations (Figure 4-3A). The average reflectance images clearly showed areas with retinal pigment epithelial detachments as well-demarcated low intensity areas that typically indicate the presence of fluid (Figure 4-3B). In phase retardation maps of the PS-SLO, the macular bow-tie patterns were observed (Fig 4-3C). The depolarized light images, similar to the average reflectance images, indicated pigment epithelial detachments surrounded by fluid, but there was neither extensive pigment mottling of the RPE nor evidence of retinal vascular anomalous complex activity indicating retinal damage (Fig 4-3D). In the intensity images of OCT B-scan, the retinal pigment epithelial detachments were clearly observed, and the microstructures of retinal layers from internal limiting membrane to retinal pigment epithelium were well-preserved (Fig 4-3E). In the B-scan cumulative phase retardation images of PS-SD-OCT, polarization scramble at the RPE layers was clearly observed, and implied that microstructures of retinal pigment epithelium were well-preserved (Fig 4-3F). This polarization scramble was also detected in the *en face* retardation image of PS-SD-OCT (Fig 4-3G). In other retinal layers, retardations were low and constant throughout the retinas except RPE layers, and there were no obvious abnormal birefringence at the retinal pigment epithelial detachments in the PS-SD-OCT images.

We evaluated the 3 cases of early stage of exudative AMD with predominantly classic CNVs (Table 1, Fig 4-4). All patients noticed visual disturbances no more than two months before the test. The fluorescein angiograms demonstrated the areas of leakages (Figure 3A). The average reflectance images of the PS-SLO visualized the fluids in CNVs as low intensity areas, with the surrounding exudates as bright features (Fig 4-4B). Macular bow-tie patterns in the phase retardation maps of the PS-SLO were observed; however, the contours were somewhat disrupted at the areas with exudation (Figure 4-4C). The depolarized light images visualized CNVs as high intensity areas surrounded by low intensity areas (Fig 4-4). The intensity images of B-scan OCT showed CNVs as high-reflective lesions that elevated the overlying retinas, and the RPE layers were disrupted in a corresponding manner (Figure 4-4E). CNVs had low birefringence in the cumulative phase retardation images of B-scan PS-SD-OCT (Fig 4-4F). This implies that the CNV contained only a small fibrotic change, since increased amounts of proteins such as collagen

or fibrin provide a strong birefringence signal well-known in wound-healing. Cumulative phase retardation values at the CNVs were distributed from 20 deg to 42 deg. The RPE layers were disrupted to varying degrees, but the depths of the layers were fairly uniform, while the elevations of the overlying retinas varied greatly. The comparison of the left and right portions of the lesion, and also the RPE beneath the flatter portion vs. the more sloped portions of the lesion, indicates that the changes shown for the deeper layers did not result solely from the signal being blocked by the different pathological structures through the fluid associated with the lesion (Fig 4-4E, F). These findings implied that the microstructure of retinal pigment epithelium was damaged to varying degrees beneath the lesion.

We evaluated a case of CNV with RPE tear (Table 1, Figure 4-5). Indocyanine angiography clearly showed the RPE tear as a hypofluorescent area adjacent to CNV (Fig 4-5A). The average reflectance images and the depolarized light image of PS-SLO showed the RPE tear as a high intensity area, consistent with previous near infrared imaging (Fig 4-5B, D). In the depolarized light image, an area of CNV was shown as a spotted high intensity area (Fig 4-5D), and the CNV and RPE tear were surrounded by low intensity area. The macular bow-tie pattern in the phase retardation map of the PS-SLO was somewhat disrupted in the area with exudation (Fig 4-5C). The intensity image of the B-scan OCT showed the CNV as a high-reflective lesion, and this lesion had low birefringence in the PS-SD-OCT image (Figs 4-5E, F). The cumulative phase retardation value at the CNV was 31 deg. The RPE tear could be observed in the inferior to superior intensity image of B-scan OCT, and was clearly demonstrated as a discontinuity of intensity and of polarization scramble in PS-SD-OCT images (Figures 4-5G, H).

We evaluated 3 cases of the end stage of exudative AMD with disciform scars (Table 1, Figure 4-6). The color images showed the light scattering properties of scars (Figure 4-6A). The average reflectance images of the PS-SLO showed the disciform scars as high intensity areas demarcated with neighboring low intensity areas (Figure 4-6B). In the phase retardation maps of the PS-SLO, abnormal strong birefringence at the disciform scars were observed (Figure 4-6C), but no obvious macular bow-tie. The depolarized light images showed disciform scars as low intensity areas that included smaller bright regions, surrounded by pigment changes (Figure 4-6D). In the intensity images of B-scan OCT, high reflective layers were observed in deep retinal layers, and the RPE layers were hardly distinguishable (Figure 4-6E). In the phase retardation images of B-scan PS-SD-OCT, areas of abnormal birefringence were observed corresponding to these high reflective layers, and polarization scramble at the RPE layer could not be detected (Figure 4-6F). Cumulative phase retardation values at the CNVs were distributed from 115 deg to 127 deg. In the cut-away volumes of phase retardation images of PS-SD-OCT, there were sharp changes across the retinas that were not seen in normal eyes (Figure 4-6G). The areas with

abnormal birefringence corresponded to the areas with disciform scars and areas with abnormal birefringence in PS-SLO images.

In an eye with recurrence after photodynamic therapy, two distinctive exudative lesions were observed in the color fundus photograph (Table 1, Figure 4-7A). One was a disciform scar and another one was a new exudative lesion, as demonstrated by fluorescein angiography (Figure 4-7B). The polarization properties of these exudative lesions were completely different. The average reflectance image of PS-SLO showed the disciform scar as high intensity area and the new exudative lesion as a low intensity area (Figure 4-7C). In the phase retardation map, the disciform scar had a clear-cut region of strong birefringence, and the new lesion showed only weak birefringence. No macular bow-tie was present (Figure 4-7D). In the depolarized light image, the margin of the new lesion could be detected, and a choroidal vessel could be visualized in the area with the disciform scar (Figure 4-7E). In the intensity image of B-scan OCT, both lesions appeared as high reflective areas, and did not clearly distinguish the contents of two lesions (Figure 4-7F). The phase retardation image of the B-scan PS-SD-OCT clearly distinguished the contents of two lesions. The area with the disciform scar showed clearly abnormal birefringence, while the new exudative lesion showed only subtle birefringence differences from the surrounding retina (Figure 4-7G). The cumulative phase retardation value at the new CNV was 39 deg, but at the scar was 137 deg. The polarization scramble at the RPE layer was difficult to detect. In the cut-away volume of phase retardation images of PS-SD-OCT, again strong changes were found across the retina (Figure 4-7H). The area with abnormal birefringence corresponded to the area with disciform scar and area with abnormal birefringence in PS-SLO image.

We compared the mean cumulative phase retardation across patients, with the lesions that occurred within two months in one group (cases 6-9) and the older disciform scars in another group (cases 10-12). The retardation values at the disciform scars were significantly higher than CNVs ( $P = 0.020$ , Mann-Whitney U test, Figure 4-8).

## **4-6. Discussion and Conclusion**

In this study, we compared PS-SLO images and PS-SD-OCT images, and evaluated polarization analysis as a non-invasive technique for the investigation of the stages of exudative AMD. In the polarization image of AMD, striking polarization changes were observed at the disciform scars in both PS-SLO images and PS-SD-OCT images. Areas of these polarization changes were consistent across the two systems. Retardation values at disciform scars were significantly higher than at recent CNVs. The polarization scramble at the RPE layer in PS-SD-OCT images was disrupted to various degrees, as expected by the location and severity of the pathological changes. The borders of well-defined CNV could

be clearly detected in the depolarized light image<sup>22</sup>.

These polarimetry findings provide the information about the microstructure of the retina. Variation in the molecular compositions of the lesion components, and which tissues provide the strongest birefringence signal, are two factors in polarization changes in light returning from the retinas of eyes with exudative AMD. Disciform scarring in exudative AMD contains an abnormal fibrotic change. These fibrotic changes are composed of proteins that demonstrate birefringent properties<sup>56</sup>. In the early stage of exudative AMD, this fibrotic change is not prominent, and only a small birefringence change at the exudation could be observed. This polarimetry finding is useful in the evaluation the microstructures at the high-reflective layer in OCT images, as shown in the cases of disciform scar with new exudative lesions. The phase retardation image of PS-SD-OCT could discriminate polarization properties of two lesions, while the intensity image of OCT could not discriminate the contents of two lesions. PS-SD-OCT could provide useful information about the microstructure of exudative lesion, which could not be provided by the conventional intensity-based OCT. Polarimetry imaging also provides the information about the integrity of the microstructure of the retina. Polarization scramble at the RPE layer in PS-SD-OCT implies that microstructures of the RPE were well-preserved, and could be used as the optical signature of an intact RPE, against which an RPE tear could be compared and thus detected. Polarimetry imaging provided the additional information that could not be obtained with conventional *en face* imaging or OCT.

PS-SD-OCT has the potentiality to evaluate the polarization properties of macular disease. Three-dimensional information of the intensity and the polarimetry were obtained, and provided similar *en face* information as PS-SLO phase retardation maps. However, PS-SD-OCT is in still the development stage, and not commercially available. Maintenance and operation are more complicated compared to commercialized OCT. The PS-SLO is a commercially available system, and has a long and continuing literature for clinical application in glaucoma<sup>48</sup>. A practical advantage of PS-SLO over PS-SD-OCT is that the testing time of PS-SLO (0.7 s) is shorter than that of PS-SD-OCT (5.5 s). The PS-SLO is an effective system for easily obtaining the polarization state at the region of interest, and provides information concerning multiply scattered light as well as birefringence. With PS-SD-OCT, the origin of the polarization change could be readily detected, and could provide more information about polarization properties of retinal disease. A combination of PS-SLO and PS-SD-OCT is an effective tool to understand the polarization properties of the retinal disease.

## **4-7. Summary**

We compared the information from two techniques and investigate how they complement each other, polarization-sensitive scanning laser ophthalmoscope (PS-SLO) images and polarization-sensitive spectral-domain optical coherence tomography (PS-SD-OCT) images. We prospectively examined the eyes of two healthy subjects and 13 patients with exudative age-related macular degeneration (AMD). Both PS-SLO and PS-SD-OCT images detected abnormal birefringence at the locus of exudative lesions. PS-SD-OCT images showed that in the old lesions with fibrosis, phase retardation values were significantly larger than in new lesions ( $P = 0.020$ ). Increased scattered light and altered polarization scramble were associated with portions of the lesions. PS-SLO and PS-SD-OCT are complementary in probing birefringence properties in exudative AMD. Polarimetry findings in exudative AMD emphasized different features, and were related to the progression of the disease, potentially providing a non-invasive tool for microstructure

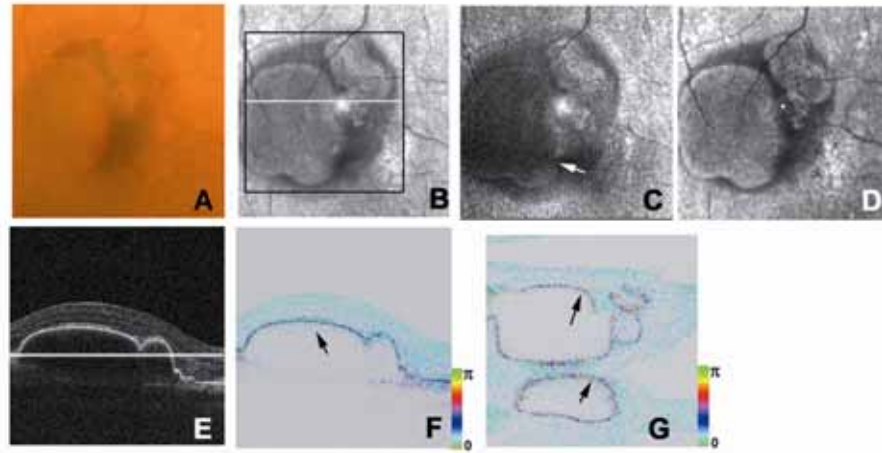


Figure 4-3

Right eye of a 72-year-old female with pigment epithelial detachment. (A) Color fundus photograph. (B) Average reflectance image of GDx. The black line indicates the area of PS-SD-OCT imaging, and the white line indicates the scanning line of PS-SD-OCT in Figs. 4-3E and 4-3F. A bright spot on the center of the GDx image was an instrument artifact. (C) Phase retardation map of GDx. The white arrow indicates the center of the macular bow-tie. (D) Depolarized light image of GDx. (E) B-scan intensity image of PS-SD-OCT. The white line indicates the plane for *en face* image in Fig. 4-3G. (F) B-scan cumulative phase retardation image. The black arrow indicates the polarization scramble at the RPE layer. (G) *En face* cumulative phase retardation image. The black arrows indicate the polarization scramble at the RPE layer.

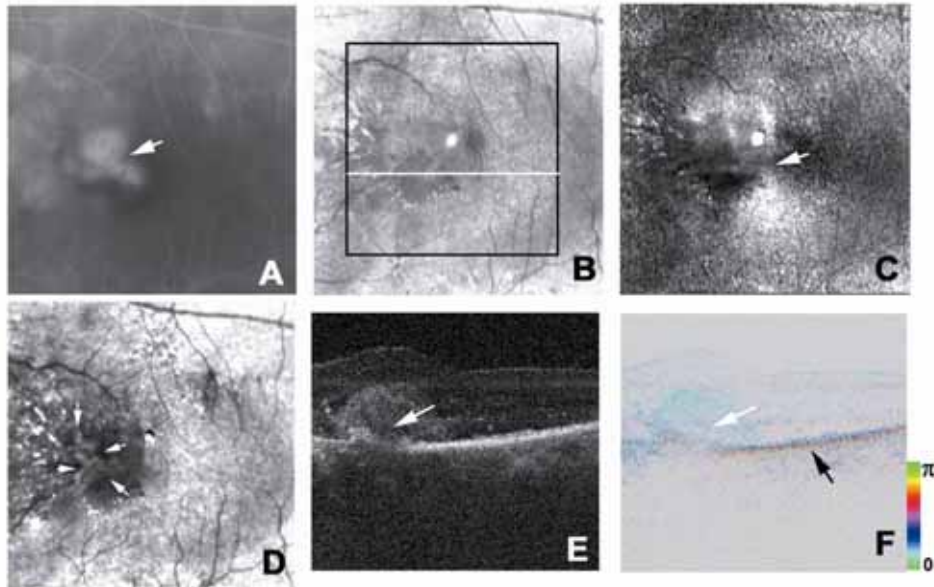


Figure 4-4

Left eye of a 75-year-old male with early stage of exudative AMD with predominantly classic CNV. **(A)** Fluorescein angiography image. The white arrow indicates CNV. **(B)** Average reflectance image of GDx. The black line indicates the area of PS-SD-OCT imaging, and the white line indicates the scanning line of PS-SD-OCT in Figs. 4-4E and 4-4F. A bright spot on the center of the GDx image was an instrument artifact. **(C)** Phase retardation map of the GDx. The white arrow indicates the center of macular bow-tie appearance. **(D)** Depolarized light image of GDx. The white arrows indicate the high-intensity area corresponding to the CNV. **(E)** B-scan intensity image of PS-SD-OCT. The white arrow indicates the high-reflective layer corresponding to the CNV. **(F)** B-scan cumulative phase retardation image. The white arrow indicates the layer corresponding to the CNV, and the black arrow indicates the polarization scramble at the RPE layer.

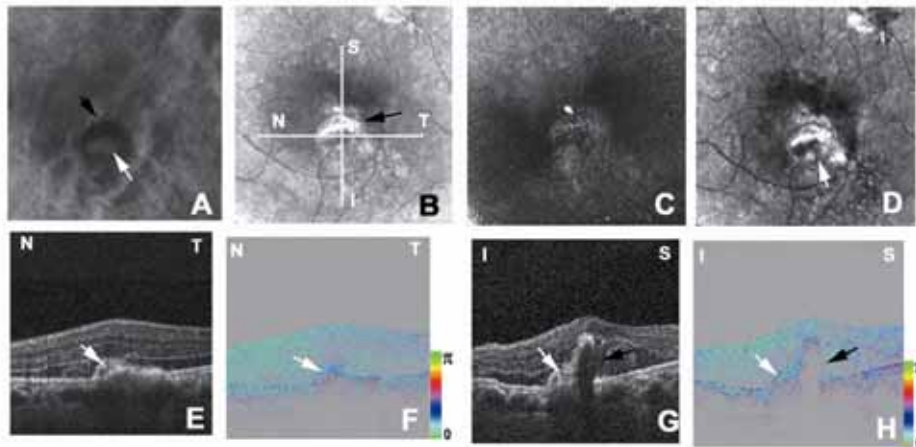


Figure 4-5

Left eye of a 57-year-old male with exudative AMD with RPE tear. **(A)** Indocyanine green angiography image. The black arrow indicates the RPE tear, and the white arrow indicates CNV. **(B)** Average reflectance image of GDx. The black arrow indicates the RPE tear. The white lines indicate the scanning lines of PS-SD-OCT in Figs. 4-5E, 4-5F, 4-5G, and 4-5H. A bright spot on the center of the GDx image was an instrument artifact. **(C)** Phase retardation map of GDx. **(D)** Depolarized light image of GDx. The white arrow indicates spotted high intensity area corresponding to the CNV. **(E)** Horizontal B-scan intensity image of PS-SD-OCT. The white arrow indicates the high-reflective layer corresponding to the CNV. **(F)** Horizontal B-scan phase retardation image of PS-SD-OCT. The white arrow indicates the CNV. **(G)** Vertical B-scan intensity image of PS-SD-OCT. The black arrow indicates the RPE tear, and the white arrow indicates the CNV. **(H)** Vertical B-scan phase retardation image of PS-SD-OCT. The black arrow indicates the RPE tear, and the white arrow indicates the CNV.



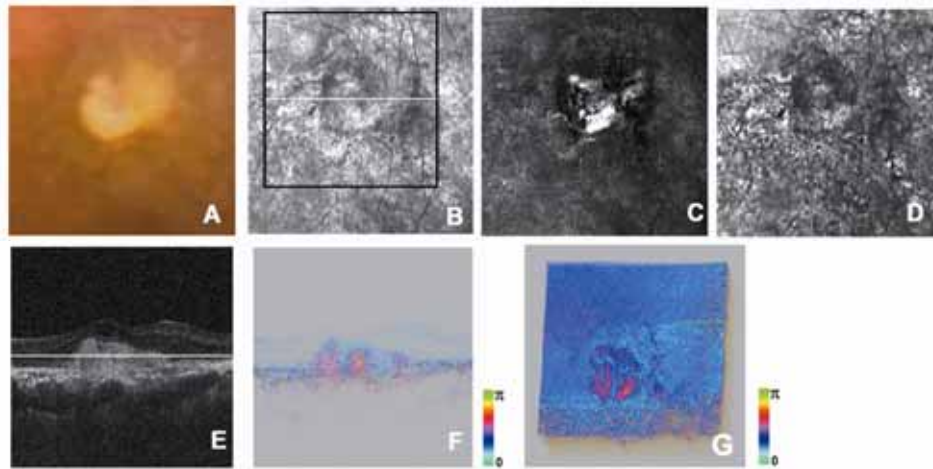


Figure 4-6

Left eye of a 75-year-old male with late stage of exudative AMD with disciform scar. (A) Color fundus photograph. (B) Average reflectance image of GDx. The black line indicates the area of PS-SD-OCT imaging, and the white line indicates the scanning line of PS-SD-OCT in Figs. 4-6E, 4-6F, and 4-6G. A bright spot on the center of the GDx image was an instrument artifact. (C) Phase retardation map of GDx. (D) Depolarized light image of GDx. (E) B-scan intensity image of PS-SD-OCT. The white line indicates the plane for cut-away volume image in 4-6G. (F) B-scan cumulative phase retardation image. (G) Cut-away volume image of cumulative phase retardation image.

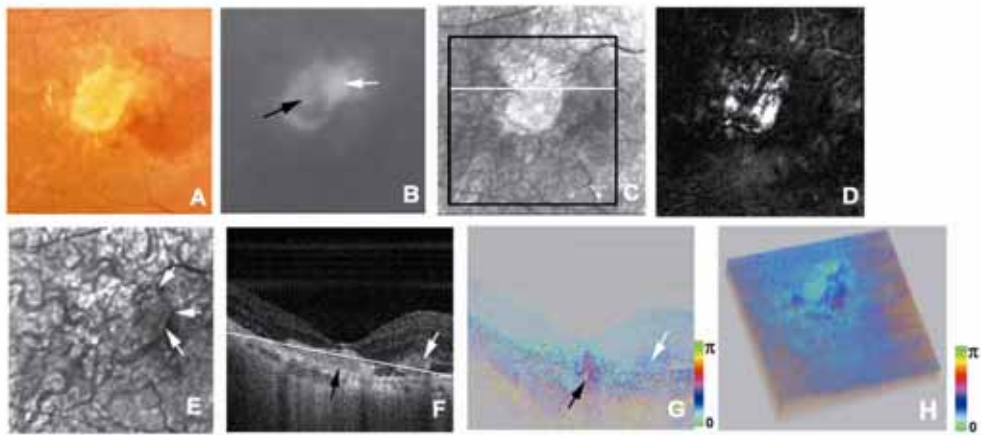


Figure 4-7

Right eye of a 66-year-old male with disciform scar with new exudative lesion. **(A)** Color fundus photograph. **(B)** Fluorescein angiography image showed a new CNV (white arrow) adjacent to the disciform scar (black arrow). **(C)** Average reflectance image of GDx. The black line indicates the area of PS-SD-OCT imaging, and the white line indicates the scanning line of PS-SD-OCT in Figs. 4-7F, 4-7G, and 4-7H. A bright spot on the center of the GDx image was an instrument artifact. **(D)** Phase retardation map of GDx. **(E)** Depolarized light image of GDx. The white arrows indicate new CNV. **(F)** B-scan intensity image of PS-SD-OCT. The white arrow indicates new CNV, and the black arrow indicates disciform scar. The white line indicates the plane for cut-away volume image in Fig. 4-7H. **(G)** B-scan cumulative phase retardation image. The white arrow indicates new CNV, and the black arrow indicates disciform scar. **(H)** Cut-away volume image of cumulative phase retardation image.

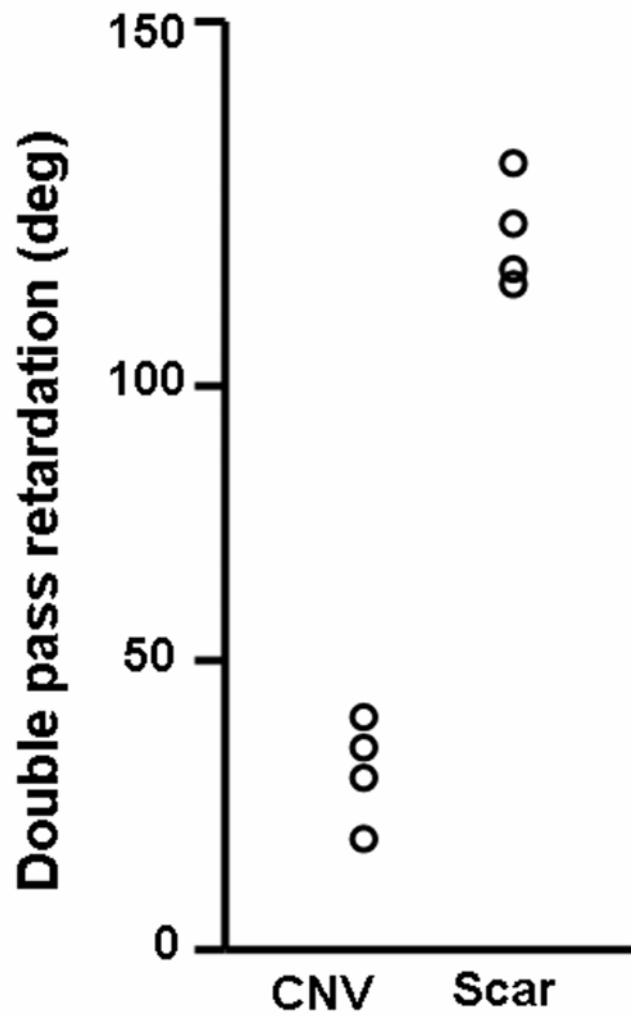


Figure 4-8  
The mean cumulative phase retardation values at the CNVs that occurred within two months before the test, and the values at the disciform scars.



# Chapter 5

## Conclusion

We evaluated the polarization properties of the human eye in vivo using PS-SLO and PS-OCT. The polarimetric findings provide information on the microstructure of the human eye.

With PS-SS-OCT, the boundary of the sclera could be easily distinguished, and the thickness of the sclera could be accurately measured. In the eye with necrotizing scleritis, birefringence at the sclera was low in diffuse areas; this implied that diffuse destruction of the collagen fibers had occurred in the sclera. The thickness of the sclera in the eye with necrotizing scleritis was markedly low as compared to that of the sclera in the normal eyes. Destruction of collagen fibers and thinning of the sclera are important indicators of the severity of scleritis, and PS-SS-OCT could be an ideal tool for evaluating the pathological changes in the sclera.

We evaluated the polarization properties of the human retina with PS-SLO. Polarization analysis facilitated selective emphasis on different features of the retina, visualizing more superficial layers depending on the polarization content. In the depolarized light image, the leakage areas in central serous chorioretinopathy resented as high-intensity areas, indicating a high degree of multiple scattering of the returning light at those locations, which in turn suggests the presence of a local tissue disorder. Next, we studied a polarimetry method for examining retinal blood vessels in a retinal area containing epiretinal membrane. In normal eyes, the contrast between retinal arteries and veins was higher in 514-nm images. In the presence of membrane formation on the retinal surface, interference was observed in the 514-nm polarization-insensitive retinal vascular images; however, depolarized light images clearly depicted the retinal vasculature. This result suggests that polarimetric methods are an effective tool for visualizing retinal vessels in eyes with retinal disease.

We evaluated the polarization properties of the human retina with a combination of PS-SLO and PS-OCT. The PS-SLO is an effective system for easily obtaining the polarization state at the region of interest, and provides information on multiple-scattered light as well as birefringence. With PS-SD-OCT, the origin of the polarization change could be easily detected and more information was available on the polarization properties of the diseased retina. A combination of PS-SLO and PS-SD-OCT is an effective tool for understanding the polarization properties of the retina.

From the results of this study, we confirmed that polarimetric imaging is an effective technique for evaluating the microstructure of the human eye.

# References

1. Berendschot TT, DeLint PJ, van Norren D. Fundus reflectance--historical and present ideas. *Prog Retin Eye Res.* 2003;22:171-200.
2. Delori FC, Gragoudas ES. Examination of the ocular fundus with monochromatic light. *Ann Ophthalmol* 1976;8:703-709.
3. van de Kraats J, Berendschot TT, van Norren D. The pathways of light measured in funds reflectometry. *Vision Res* 1996;36:2229-2247.
4. Bour LJ. Polarized light and the eye. In: Charman WN, ed. *Visual Optics and Instrumentation*. Boca Raton, FL: CRC Press, 1981:310-325.
5. Dreher AW, Reiter K, Weinreb RN. Spatially resolved birefringence of the retinal nerve fiber layer assessed with a retinal laser ellipsometry. *Applied Optics* 1992;31:3730-3735.
6. Cense B, Chen TC, Park BH, Pierce MC, de Boer JF. Thickness and birefringence of healthy retinal nerve fiber layer tissue measured with polarization-sensitive optical coherence tomography. *Invest Ophthalmol Vis Sci.* 2004;45:2606-2612.
7. Yamanari M, Miura M, Makita S, Yatagai T, Yasuno Y. Phase retardation measurement of retinal nerve fiber layer by polarization-sensitive spectral-domain optical coherence tomography and scanning laser polarimetry. *J Biomed Opt.* 2008;13:014013.
8. de Boer JF, Milner TE. Review of polarization sensitive optical coherence tomography and Stokes vector determination. *J Biomed Opt.* 2002;7:359-371.
9. Watson PG, Young RD. Scleral structure, organisation and disease. A review. *Exp Eye Res.* 2004;78:609-623.
10. Heiligenhaus A, Schilling M, Lung E, Steuhl KP. Ultrasound biomicroscopy in scleritis. *Ophthalmology.* 1998;105:527-534.
11. Radhakrishnan S, Rollins AM, Roth JE, Yazdanfar S, Westphal V, Bardenstein DS,

Izatt JA. Real-time optical coherence tomography of the anterior segment at 1310 nm. *Arch Ophthalmol.* 2001;119:1179-1185.

**12.** B. Baumann EGMP, Hitzenberger CK, Cense B, Nassif NA. Single camera based spectral domain polarization sensitive optical coherence tomography  
Ultrahigh-resolution high-speed retinal imaging using spectral-domain optical coherence tomography. *Optics Express* 2007;15:1054-1063.

**13.** Park BH, Pierce MC, Cense B, de Boer JF. Jones matrix analysis for a polarization-sensitive optical coherence tomography system using fiber-optic components. *Opt Lett* 2004;29:2512-2514.

**14.** Wojtkowski M, Bajraszewski T, Targowski P, Kowalczyk A. Real-time in vivo imaging by high-speed spectral optical coherence tomography. *Opt Lett* 2003;28:1745-1747.

**15.** Yasuno Y, Madjarova VD, Makita S, Akiba M, Morosawa A, Chong C, Sakai T, Chan K, Itoh M, Yatagai T. Three-dimensional and high-speed swept-source optical coherence tomography for in vivo investigation of human anterior segments. *Optics express* 2005;13:10652-10664.

**16.** Miura M, Mori H, Watanabe Y, Usui M, Kawana K, Oshika T, Yatagai T, Yasuno Y. Three-dimensional optical coherence tomography of granular corneal dystrophy. *Cornea.* 2007;26:373-374.

**17.** Miura M, Kawana K, Iwasaki T, Kiuchi T, Oshika T, Mori H, Yamanari M, Makita S, Yatagai T, Yasuno Y. Three-dimensional anterior segment optical coherence tomography of filtering blebs after trabeculectomy. *J Glaucoma.* 2008;17:193-196.

**18.** Hammer M, Roggan A, Schweitzer D, Muller G. Optical properties of ocular fundus tissues--an in vitro study using the double-integrating-sphere technique and inverse Monte Carlo simulation. *Phys Med Biol* 1995;40:963-978.

**19.** Van Norren D, Tiemeijer LF. Spectral reflectance of the human eye. *Vision Res* 1986;26:313-320.

**20.** Bueno JM. Polarimetry in the human eye using an imaging linear polariscope. *J Opt*



A: *Pure Appl Opt* 2002;4:553 - 561.

21. Burns SA, Elsner AE, Mellem-Kairala MB, Simmons RB. Improved contrast of subretinal structures using polarization analysis. *Invest Ophthalmol Vis Sci* 2003;44:4061-4068.
22. Elsner AE, Weber A, Cheney MC, VanNasdale DA, Miura M. Imaging polarimetry in patients with neovascular age-related macular degeneration. *J Opt Soc Am A Opt Image Sci Vis.* 2007;24:1468-1480.
23. Weber A, Elsner AE, Miura M, Kompa S, Cheney MC. Relationship between foveal birefringence and visual acuity in neovascular age-related macular degeneration. *Eye.* 2007;21:353-361..
24. Gass JDM. Stereoscopic atlas of macular disease, 3rd edition. St. Lois, Washington, D.C., Toronto: Mosby, 1987:46-59.
25. von Ruckmann A, Fitzke FW, Fan J, Halfyard A, Bird AC. Abnormalities of fundus autofluorescence in central serous retinopathy. *Am J Ophthalmol* 2002;133:780-786.
26. Yannuzzi LA, Rohrer KT, Tindel LJ, Sobel RS, Costanza MA, Shields W, Zang E. Fluorescein angiography complication survey. *Ophthalmology* 1986;93:611-617.
27. Hee MR, Puliafito CA, Wong C, Reichel E, Duker JS, Schuman JS, Swanson EA, Fujimoto JG. Optical coherence tomography of central serous chorioretinopathy. *Am J Ophthalmol* 1995;120:65-74.
28. Iida T, Hagimura N, Sato T, Kishi S. Evaluation of central serous chorioretinopathy with optical coherence tomography. *Am J Ophthalmol* 2000;129:16-20.
29. Montero JA, Ruiz-Moreno JM. Optical coherence tomography characterisation of idiopathic central serous chorioretinopathy. *Br J Ophthalmol* 2005;89:562-564.
30. Levine R, Brucker A, Robinson F. Long-term follow-up of idiopathic central serous chorioretinopathy by fluorescein angiography. *Ophthalmology* 1989;96:854-859.
31. Schatz H, McDonald HR, Johnson RN, Chan CK, Irvine AR, Berger AR, Folk JC,

Robertson DM. Subretinal fibrosis in central serous chorioretinopathy. *Ophthalmology* 1995;102:1077-1088.

**32.** Knighton RW, Huang XR, Greenfield DS. Analytical model of scanning laser polarimetry for retinal nerve fiber layer assessment. *Invest Ophthalmol Vis Sci* 2002;43:383-392.

**33.** Gass JDM. Stereoscopic atlas of macular disease. St. Louis, Washington, D. C., Toronto: Mosby, 1987: 938-951.

**34.** Ogura Y, Honda Y. Evaluation of idiopathic epiretinal membranes by a scanning laser ophthalmoscope. *Br J Ophthalmol* 1993;77:534-535.

**35.** Rizzo S, Genovesi-Ebert F, Murri S, Belting C, Vento A, Cresti F, Manca ML. 25-gauge, sutureless vitrectomy and standard 20-gauge pars plana vitrectomy in idiopathic epiretinal membrane surgery: a comparative pilot study. *Graefes Arch Clin Exp Ophthalmol*. 2006;244:472-479.

**36.** Patton N, Aslam TM, MacGillivray T, Deary IJ, Dhillon B, Eikelboom RH, Yogesan K, Constable IJ. Retinal image analysis: concepts, applications and potential. *Prog Retin Eye Res*. 2006;25:99-127.

**37.** Hammer M, Leistriz S, Leistriz L, Schweitzer D. Light paths in retinal vessel oxymetry. *IEEE Trans Biomed Eng*. 2001;48:592-598.

**38.** Park R, Twietmeyer K, Chipman R, Beaudry N, Salyer D. Wavelength dependence of the apparent diameter of retinal blood vessels. *Appl Opt* 2005;44:1831-1837.

**39.** Delori FC, Gragoudas ES, Francisco R, Pruett RC. Monochromatic ophthalmoscopy and fundus photography. The normal fundus. *Arch Ophthalmol* 1977;95:861-868.

**40.** Elsner AE, Burns SA, Hughes GW, Webb RW. Reflectometry with a scanning laser ophthalmoscope. *Applied optics* 1992;31:3697-3710.

**41.** Kirkpatrick JN, Manivannan A, Gupta AK, Hipwell J, Forrester JV, Sharp PF. Fundus imaging in patients with cataract: role for a variable wavelength scanning laser ophthalmoscope. *Br J Ophthalmol*. 1995;79:892-899.

- 42.** Elsner AE, Burns SA, Delori FC, Webb RH. Quantitative Reflectometry with the SLO. In: Nasemann JE, Burk ROW, eds. *Laser Scanning Ophthalmoscopy and Tomography*. Berlin: Quintessenz-Verlag, 1990:109-121.
- 43.** Bartsch DU, Freeman WR. Laser-tissue interaction and artifacts in confocal scanning laser ophthalmoscopy and tomography. *Neurosci Biobehav Rev* 1993;17:459-467.
- 44.** Weber A, Cheney MC, Smithwick QYJ, Elsner AE. Polarimetric imaging and blood vessel quantification. *Optics Express* 2004;12:5178-5190.
- 45.** Miura M, Elsner A. Three dimensional imaging in age-related macular degeneration. *Optics Express* 2001;9:436-443.
- 46.** Elsner AE, Miura M, Stewart JB, Kairala MB, Burns SA. Novel algorithms for polarization imaging resulting in improved quantification of retinal blood vessels. *Stud Health Technol Inform* 2003;94:59-61.
- 47.** Demos SG, Alfano RR. Optical polarization imaging. *Appl Opt* 1997;36:150-155.
- 48.** Zhou Q, Weinreb RN. Individualized Compensation of Anterior Segment Birefringence during Scanning Laser Polarimetry. *Invest Ophthalmol Vis Sci* 2002;43:2221-2228.
- 49.** Elsner A, Burns S, Weiter J, Delori F. Infrared imaging of sub-retinal structures in the human ocular fundus. *Vision Res* 1996;36:191-205.
- 50.** Huang D, Swanson E, Lin C, Schuman J, Stinson W, Chang W, Hee M, Flotte T, Gregory K, Puliafito C, Fujimoto J. Optical coherence tomography. *Science* 1991;254:1178-1181.
- 51.** Hee MR, Huang EA, Swanson EA, Fujimoto JG. Polarization-sensitive low-coherence reflectometer for birefringence characterization and ranging. *J. Opt. Soc. Am. B* 1992;9:903-908.
- 52.** Pircher M, Gotzinger E, Findl O, Michels S, Geitzenauer W, Leydolt C, Schmidt-Erfurth U, Hitzenberger CK. Human macula investigated in vivo with

polarization-sensitive optical coherence tomography. *Invest. Ophthalmol. Vis. Sci.* 2006;47:5487-5494.

**53.** Gotzinger E, Pircher M, Hitzenberger CK. High speed spectral domain polarization sensitive optical coherence tomography of the human retina. *Opt. Express* 2005;13:10217-10229.

**54.** Y. Yasuno SMYSMI, Yatagai T. Birefringence imaging of human skin by polarization-sensitive spectral interferometric optical coherence tomography. *Optics Letters* 2002;27:1803-1805.

**55.** Klein R, Klein BE, Linton KL. Prevalence of age-related maculopathy. The Beaver Dam Eye Study. *Ophthalmology* 1992;99:933-943.

**56.** de Boer JF, Milner MJ, van Gemert JC, Nelson JS. Two-dimensional birefringence imaging in biological tissue by polarization-sensitive optical coherence tomography. *Opt. Lett* 1997;22:934-936.

# Curriculum vitae

- 1960: Born in Shizuoka, Japan
- 1976–1979: Numazu-Higashi High School
- 1979–1985: School of Medicine, Nippon Medical School
- 1985: Bachelor of Medicine, Nippon Medical School
- 1985: License to practice medicine
- 1991: Title of Medical Specialist in Ophthalmology
- 1992: Doctoral Degree in Medicine, Nippon Medical School
- 1995: Assistant Professor in Ophthalmology, Nippon Medical School
- 1997–2001: Postdoctoral fellow at the Schepens Eye Research Institute and Harvard Medical School
- 2003: Assistant Professor in Ophthalmology, Tokyo Medical University
- 2007: Visiting research fellow, Institute of Applied Physics, University of Tsukuba
- 2009: Associate Professor in Ophthalmology, Tokyo Medical University
- 2008 to the present: Doctoral course at a Graduate School, Institute of Applied Physics, University of Tsukuba

